Author/s:
Deuse, Mathieu Maurice P

Title:
High-fidelity numerical investigation of different mechanisms of aerofoil self-noise

Date:
2020

Persistent Link:
https://hdl.handle.net/11343/238524

High-fidelity numerical investigation of different mechanisms of aerofoil self-noise

Mathieu Deuse
ORCID: 0000-0001-6934-1303

Master of Philosophy

January 2020

The University of Melbourne,
Melbourne School of Engineering,
Department of Mechanical Engineering

Submitted in total fulfilment for the degree of Master of Philosophy

Abstract

The self-noise of an isolated controlled-diffusion aerofoil is investigated using direct noise computations. The motivation is to investigate the multiple sources of aerofoil self-noise on a realistic compressor blade geometry, the physical mechanisms leading to the generation of sound, and the influence of compressibility effects. The use of direct noise computation allows to obtain a detailed and accurate picture of both the hydrodynamic and acoustic fields.

The high-order finite difference solver HiPSTAR is used to conduct the numerical simulations. In the context of the present study, the capabilities of HiPSTAR have been extended with an overset grid framework. The framework employs a novel algorithm for the generation of the composite grid, i.e. to identify the discretisation, interpolation and non-physical points. This algorithm was designed to minimise and simplify the user input, while maintaining the flexibility to handle complex setups. An explicit fourth-order Lagrange interpolation scheme is used, so that the formal order of accuracy of the finite difference scheme used in the flow solver is matched. An instability linked to the possible presence of uncoupled numerical solutions on separate grids sharing the same physical location is discussed, and a modification of the composite grid generation algorithm that prevents this instability is introduced. The final overset grid method is validated with two test cases: the convection of an isentropic vortex and the Taylor-Green vortex.

The solver is used to conduct four large eddy simulations and one direct numerical simulation of the flow around the controlled-diffusion aerofoil. The angle of attack is $8°$, the chord-based Reynolds number is 10^5, and results obtained for four values of the free-stream Mach number $[0.2, 0.3, 0.4, 0.5]$ are compared. For those flow parameters, the pressure side is fully laminar, whereas a separation bubble is present on the suction side close to the leading edge that promotes transition to turbulence. The size of the separation bubble is found to increase with the Mach number. Two noise sources are observed, one at the trailing edge and one in the leading edge transition/reattachment region. The first has a broadband, low frequency spectrum, while the second displays a tone whose frequency depends on the local Mach number. Because the leading edge separation bubble is very small, the associated tone frequency is high and requires a significantly finer grid to faithfully resolve the acoustic propagation than what is typically deemed sufficient. Finally, cross correlations between the surface pressure and the far-field pressure reveal that the pressure fluctuations reaching the trailing edge are initially generated in the transition/reattachment region, which indicates that the trailing edge noise is a consequence of the pressure fluctuations generated by the separation bubble.

Contents

Acknowledgements

I would like to thank my first thesis supervisor Professor Richard D. Sandberg for the excellent guidance throughout all this study. I would also like to thank Professor Ivan Marusic for co-supervising my project. Thank you as well to all my colleagues at the University of Melbourne for the advice and helpful discussions. Finally, I am grateful for the scholarship provided by the University of Melbourne.

Chapter 1

Introduction

1.1 Context

With the omnipresence of technology and the increasing growth of transport, our environment is becoming noisier and noisier. One major contributor to environmental noise pollution is aerofoil noise, which results from the unsteady flow around an aerofoil. Not only does aerofoil noise impact our health (it has been identified as a global public health problem by the World Health Organisation [1]), but it also has important economical consequences, in particular in the context of air transport where stringent regulation applies to aircraft noise, with noisier aircraft being subject to higher fees [2].

One contributor to aerofoil noise is the aerofoil self-noise, defined as the noise produced by the interaction between the aerofoil blade and the pressure fluctuations in its boundary layer and wake. The aerofoil self-noise is of particular interest as it defines the minimum noise level that is generated by a given geometry without incoming flow perturbations or installation effects [3]. The aerofoil Trailing-Edge (TE) plays an important role in aerofoil self-noise production: according to Brooks et al. [4], the TE is responsible for four of the five mechanisms that radiate noise. Moreover, TE noise dominates the total noise for a large range of applications such as aircraft engines [5] and high-lift devices [6], wind turbines [7], and industrial and domestic ventilation systems [8].

As noise reduction technologies are evolving rapidly [5], it is crucial to be able to accurately predict aerofoil self-noise, and to understand the physical mechanisms leading to its production. In the context of industrial applications, prediction tools need to be fast, and thus inexpensive models are often sought. The most popular model of aerofoil noise is probably the model of Amiet [9], which predicts the far-field sound spectrum based on the aerofoil surface pressure spectrum, with the latter either obtained from (semi-)empirical models or computed using unsteady Computational Fluid Dynamics (CFD) (typically Unsteady Reynolds-Averaged Navier-Stokes (URANS) calculations for industrial applications). Amiet's model is particularly attractive due to its low computational cost, however its accuracy deteriorates at low frequencies, moreover it cannot predict the overall aerofoil self-noise if there exist other noise sources apart from the TE, as shown by Sandberg and Jones [10]. In order to improve such models, an in-depth understanding of the physical mechanisms leading to noise production is essential.

Another method for aerofoil noise prediction that has been getting more and more attention during the last decade is Direct Noise Computation (DNC). Instead of relying on an acoustic model or analogy, this approach consists in the numerical simulation of the full compressible turbulent flow, including the acoustic field. To do so, a high-fidelity CFD solver is used, either for the Direct Numerical Simulation (DNS) or Large Eddy Simulation (LES) of the flow. Although the computational cost of DNC limits the range of Reynolds numbers that can be simulated (particularly when using DNS), the recent advances in computing powers have made DNC affordable for practical moderate Reynolds number applications [11], such as small wind turbines or ventilation systems.

1.2 Direct noise simulations of aerofoil noise

The utilisation of DNC to investigate aerofoil noise dates back to 2007, and started with two-dimensional simulations of aerofoil tones. Desquesnes et al. [12] used DNS to investigate the tonal noise mechanism; they studied the two-dimensional flow over a NACA0012 aerofoil at angles of attack $\alpha = 2°$ and $5°$, moderate chord-based Reynolds numbers $\mathrm{Re} = 10^5$ and 2×10^5, and low free-stream Mach number $\mathrm{M} = 0.05$ and 0.1. The linear stability analysis they performed showed that the main tone noise frequency matched the frequency of the most amplified Tollmien-Schlichting wave on the pressure side. They explained the tone noise mechanism as a feedback loop between the boundary layer and the acoustic source. The latter is of dipolar nature, and is located in the near wake.

The same year, Sandberg et al. [13] also performed DNS of the two-dimensional flow over a NACA0012 aerofoil. Three angles of attack were considered ($\alpha = 0°$, $5°$ and $7°$), with $\mathrm{Re} = 5 \times 10^4$ and $\mathrm{M} = 0.4$. They demonstrated that although Amiet's model is suitable for the prediction of the TE noise of a finite thickness aerofoil, the prediction of far-field sound based only on the surface pressure is not applicable for all frequencies and angles of attack. In 2008, Sandberg et al. [14] extended this investigation with a three-dimensional DNS for the case $\alpha = 5°$. They found that the turbulent flow exhibits a second noise source distinct from the TE, and associated with the transition/reattachment region on the aerofoil upper surface.

Also in 2008, Marsden et al. [15] performed a three-dimensional DNC of aerofoil noise. They used LES to simulate the flow over a NACA0012 at zero incidence, at $\mathrm{Re} = 5 \times 10^5$ and $\mathrm{M} = 0.22$. They demonstrated that DNC is able to predict the noise of transitional flow with a reasonable agreement with experimental results.

In 2010 and 2011, Jones and Sandberg [16, 17] used two-dimensional DNS to investigate the role of an acoustic feedback loop for the tonal noise generation. They considered the NACA0012 aerofoil at four angles of attack ($0°$, $0.5°$, $1°$, $2°$), with $\mathrm{Re} = 10^5$ and $\mathrm{M} = 0.4$. It appeared that the tonal noise could be successfully predicted by Amiet's theory, indicating that the underlying mechanism is likely to be TE scattering, rather than a distributed source in the wake. Using a linear stability analysis, they concluded that the tonal noise occurred at a lower frequency than that of the most unstable convective wave. The explanation that they proposed is that the feedback loop selects and amplifies the frequency for which the receptivity and TE noise production mechanisms are the most efficient, which is lower than the frequency of the most unstable convective wave.

In 2011, Sanjosé et al. [18] investigated the self-noise of a Controlled-Diffusion (CD) aerofoil at $8°$ of incidence, and $\mathrm{Re} = 1.5 \times 10^5$ and $\mathrm{M} = 0.05$, using the Lattice-Boltzmann Method (LBM). Two configurations were considered: for the first configuration the aerofoil is surrounded by a uniform mean flow, whereas for the second configuration the aerofoil is embedded in a jet flow of a wind tunnel, so that the numerical setup is more representative of an existing experimental setup. The installation effects were found to significantly influence the separation bubble and the boundary layer on the suction side. They also identified a noise source close to the separation bubble, in addition to the TE noise source.

In 2012, Tam and Ju [19] performed two-dimensional DNS of the flow over a NACA0012 aerofoil with a blunt TE at zero incidence, in order to investigate the tonal noise production mechanism. They considered three different TE thicknesses. The Reynolds number range was from 2×10^5 to 5×10^5 and the Mach number range was from 0.0853 to 0.213. Using stability analysis, they showed that the tone frequency was the same as the most amplified Kelvin-Helmholtz instability in the wake. Thus they suggested that the energy source of the noise was the near-wake instability, which interacted with the TE and generated tones.

In 2012, Winkler et al. [20] performed DNS of a NACA6512-63 aerofoil at zero angle of attack, $\mathrm{Re} = 1.5 \times 10^5$ and $\mathrm{M} = 0.25$. In order to compare to available experimental results, the aerofoil was embedded in the jet of a wind tunnel: to take into account the installation effect of the wind tunnel, they used the results of a two-dimensional Reynolds-Averaged Navier-Stokes (RANS) simulation as boundary conditions for the outer boundaries of the DNS. To reproduce the early transition observed in the experiment, an immersed-boundary method was used to trip the aerofoil suction side. A close agreement was obtained between the numerical and experimental results.

In 2016, Ramírez and Wolf [21] used DNS to investigate the effect of TE bluntness on aerofoil tonal noise generation. They considered a NACA0012 aerofoil at $\alpha = 3°$, $\mathrm{Re} = 5000$, and analysed the effect of compressibility by varying the Mach number between 0.2 and 0.5. They compared DNC with a hybrid approach using the Ffowcs Williams-Hawkings (FWH) analogy [22] and showed that a blunter TE emits more noise due to an increase in the magnitude of quadrupole sources.

In 2018, Wu et al. [23] performed a three-dimensional DNS of a CD aerofoil in a wind tunnel, at $\mathrm{Re} = 1.5 \times 10^5$, $\mathrm{M} = 0.25$, and $8°$ of incidence. Similarly to Winkler et al. [20], installation effects were included by using the results of a two-dimensional RANS simulation as the outer boundary conditions of the DNS. Beside the TE noise, additional noises sources were observed at the Leading-Edge (LE) separation bubble and in the near wake.

The different configurations investigated in the aforementioned studies are summarised in Table 1.1. This highlights the fact that only a few different canonical configurations have been investigated with DNC so far. The range of flow parameters that have been studied is also limited. In particular, most investigations only have only considered a single Mach

Authors	Year	Geometry	Type	3-D	Re $\times 10^5$	M
Desquesnes et al. [12]	2007	NACA0012	DNS	No	1, 2	0.05, 0.1
Sandberg et al. [13]	2007	NACA0012	DNS	No	0.5	0.4
Sandberg et al. [14]	2008	NACA0012	DNS	Yes	0.5	0.4
Marsden et al. [15]	2008	NACA0012	LES	Yes	5	0.22
Jones and Sandberg [16]	2010	NACA0012	DNS	No	1	0.4
Sanjosé et al. [18]	2011	CD in jet	LBM	Yes	1.5	0.05
Tam and Ju [19]	2012	NACA0012	DNS	No	2–5	0.08–0.22
Winkler et al. [20]	2012	NACA6512	DNS	Yes	1.5	0.25
Ramírez and Wolf [21]	2016	NACA0012	DNS	No	0.05	0.2–0.5
Wu et al. [23]	2018	CD in jet	DNS	Yes	1.5	0.25

Table 1.1: Summary of previous DNC studies of aerofoil noise.

number, so that little is known about the influence of the compressibility effects on the aerofoil noise. Finally, most studies have been focused on the TE noise source, while the other self-noise sources have not been extensively studied.

1.3 Motivation and objectives

For practical applications, multiple different noise source mechanisms are likely to produce comparable contributions to the total aerofoil self-noise. So far, however, studies of aerofoil self-noise have often been focussed on the dipolar TE noise source, whereas little is known about other noise source mechanisms such as the laminar separation bubble, and their dependency on the flow parameters. The present study therefore aims to identify and quantify those sources and investigate the effect of the flow parameters, using DNC in order to avoid modelling uncertainties. Using DNC rather than other classical computational aeroacoustics methods allows to obtain a more detailed description of the noise source mechanisms, as an accurate description of the turbulent flow is obtained from high-fidelity simulation. Previous DNC only addressed a few different flow configurations, and their analysis have generally been limited to the range of low Strouhal numbers, associated to the TE noise. In the present investigation, it was found that the LE separation bubble generates some significantly higher frequencies than the TE noise source, and so the range of Strouhal numbers considered in the present study extends up to higher values than most of the previous investigations.

In order to be representative of real life engineering applications, the CD aerofoil geometry is considered (this aerofoil geometry is used for low speed compressor blades). Several previous studies (numerical and experimental) have already investigated the acoustics of this aerofoil geometry [3, 24–27], including some DNC [18, 23]. However, for most of those studies, the aerofoil was embedded in the jet of a wind tunnel (with the notable exception of the study of Sanjosé et al. [18], yet only 2D simulations were performed for the uniform flow case). In addition, most of those studies were mainly interested in TE noise, and the range of flow parameters that have been studied is also limited. In the present study, 3D DNC of the CD aerofoil in a uniform flow are conducted (therefore the simulations do not account for the installation effects).

The angle of attack is fixed to $\alpha = 8°$ (corresponding to the design condition for this aerofoil geometry [25]), and the Reynolds number is $\mathrm{Re} = 10^5$. The present article focusses on the compressibility effects: LES have been conducted at four values of the free-stream Mach number $\mathrm{M} = [0.2, 0.3, 0.4, 0.5]$, and a DNS has also been conducted for the case $\mathrm{M} = 0.4$ to validate the LES. Those high-fidelity simulations have been conducted with the HiPSTAR code.

Chapter 2

Governing equations and numerical method

2.1 Direct numerical simulation

The governing equations are the full compressible Navier-Stokes Equations (NSE) [28]. The NSE are made non-dimensional using the aerofoil chord length and the free-stream velocity, density and temperature as reference variables (in the following all the variables are in non-dimensional form). The dimensionless continuity, momentum and energy equations are:

$$\frac{\partial \rho}{\partial t} + \frac{\partial}{\partial x_j}(\rho u_j) = 0, \tag{2.1}$$

$$\frac{\partial}{\partial t}(\rho u_i) + \frac{\partial}{\partial x_j}\left[\rho u_i u_j + p\delta_{ij} - \tau_{ij}\right] = 0, \tag{2.2}$$

$$\frac{\partial}{\partial t}(\rho e) + \frac{\partial}{\partial x_j}\left[\rho u_j\left(e + \frac{p}{\rho}\right) + q_j - u_k\tau_{kj}\right] = 0. \tag{2.3}$$

In the equations above, the summation convention of repeated indexes holds, t and x_i denote the time and the space coordinates, δ_{ij} is the Kronecker delta symbol, and ρ and u_i are the fluid density and the velocity vector. Under the assumption that the fluid is Newtonian, and is an ideal gas with a constant ratio of the specific heats $\gamma = 1.4$, the total energy e and the pressure p are:

$$e = \frac{T}{\gamma(\gamma-1)\mathrm{M}^2} + \frac{u_k u_k}{2}, \tag{2.4}$$

$$p = \frac{\rho T}{\gamma \mathrm{M}^2}, \tag{2.5}$$

where T denotes the temperature. The stress tensor and heat-flux vector are:

$$\tau_{ij} = \frac{\mu}{\mathrm{Re}} \left(\frac{\partial u_i}{\partial x_j} + \frac{\partial u_j}{\partial x_i} - \frac{2}{3} \frac{\partial u_k}{\partial x_k} \delta_{ij} \right), \tag{2.6}$$

$$q_i = \frac{-1}{(\gamma - 1)\mathrm{M}^2} \frac{\mu}{\mathrm{Re}\,\mathrm{Pr}} \frac{\partial T}{\partial x_i}, \tag{2.7}$$

where the Prandtl number is $\mathrm{Pr} = 0.72$. The dynamic viscosity μ is obtained from the dimensionless Sutherland's law [29] with the constant $S = 0.3686$:

$$\mu = T^{3/2} \frac{1 + S}{T + S}\,. \tag{2.8}$$

2.2 Large eddy simulation

In the LES approach, the primitive variables are the filtered primitive variables from the DNS approach. For an arbitrary field $a(\vec{x}, t)$, the filtered field $\bar{a}(\vec{x}, t)$ is defined as:

$$\bar{a}(\vec{x}, t) = \int_{-\infty}^{\infty} \int_{-\infty}^{\infty} a(\vec{y}, \tau)\, G(\vec{x} - \vec{y}, t - \tau)\, \mathrm{d}\tau \mathrm{d}\vec{y}\,, \tag{2.9}$$

where G is the filtering kernel function [30]. In the context of compressible flows, the Favre filtered field $\tilde{a}$ is defined as:

$$\tilde{a} = \frac{\overline{\rho a}}{\bar{\rho}}\,. \tag{2.10}$$

Following the approach of Adumitroaie et al. [31], and introducing a subgrid-scale viscosity μ^{sgs}, the LES equations are:

$$\frac{\partial \bar{\rho}}{\partial t} + \frac{\partial}{\partial x_j}(\bar{\rho}\tilde{u}_j) = 0, \tag{2.11}$$

$$\frac{\partial}{\partial t}(\bar{\rho}\tilde{u}_i) + \frac{\partial}{\partial x_j}\left[\bar{\rho}\tilde{u}_i\tilde{u}_j + \bar{p}\delta_{ij} - \tau_{ij}\right] = 0, \tag{2.12}$$

$$\frac{\partial}{\partial t}(\bar{\rho} e) + \frac{\partial}{\partial x_j}\left[\bar{\rho}\tilde{u}_j\left(e + \frac{\bar{p}}{\bar{\rho}}\right) + q_j - \tilde{u}_k\tau_{kj}\right] = 0, \tag{2.13}$$

and the equations of state are:

$$\bar{p} = \frac{\bar{\rho}\tilde{T}}{\gamma \mathrm{M}^2}, \tag{2.14}$$

$$e = \frac{\tilde{T}}{\gamma(\gamma - 1)\mathrm{M}^2} + \frac{\tilde{u}_k\tilde{u}_k}{2}, \tag{2.15}$$

$$\mu = \tilde{T}^{3/2} \frac{1 + S}{\tilde{T} + S}\,. \tag{2.16}$$

$$\tau_{ij} = \left(\frac{\mu}{\mathrm{Re}} + \mu^{\mathrm{sgs}}\right)\left(\frac{\partial \tilde{u}_i}{\partial x_j} + \frac{\partial \tilde{u}_j}{\partial x_i} - \frac{2}{3}\frac{\partial \tilde{u}_k}{\partial x_k}\delta_{ij}\right), \tag{2.17}$$

$$q_i = \frac{-1}{(\gamma - 1)\mathrm{M}^2}\left(\frac{\mu}{\mathrm{Re}\,\mathrm{Pr}} + \frac{\mu^{\mathrm{sgs}}}{\mathrm{Pr_t}}\right)\frac{\partial \tilde{T}}{\partial x_i}, \tag{2.18}$$

where $\mathrm{Pr_t}$ denotes the turbulent Prandtl number, set as $\mathrm{Pr_t} = \mathrm{Pr} = 0.72$ in the present study. The subgrid-scale viscosity is calculated according to the Wall-Adapting Local Eddy-viscosity (WALE) model of Nicoud and Ducros [32], with the constant $C_w^2 = 0.325$. An advantage of the WALE model over some other subgrid-scale models is that C_w^2 is a true constant (i.e. its value is not modified dynamically), thus the computation of μ^{sgs} is relatively inexpensive. The WALE model has been proven to be accurate for other aerofoil flows in the context of turbomachinery applications: see for example Michelassi et al. [33] and Scillitoe et al. [34].

2.3 Numerical resolution

The NSE are solved using the in-house code HiPSTAR (High Performance Solver for Turbulence and Aeroacoustic Research). HiPSTAR is a high-order multi-block finite difference solver, designed to get the best performance out of modern supercomputer architectures [11]. It uses hybrid MPI/OpenMP parallelisation on CPU architectures, and hybrid MPI/OpenACC parallelisation for GPGPU accelerated architectures. In HiPSTAR, a reformulation of the NSE that uses generalised coordinates is solved. The physical coordinates are denoted x, y, z while the computational coordinates are ξ, η, z. It is noted that the coordinate mapping is two-dimensional, i.e. the third coordinate must be independent of the two other coordinates, and so z is both the physical and computational coordinate for the third dimension. For the numerical resolution of the NSE, Eqs. (2.1) to (2.3) are reformulated as follows:

$$\frac{\partial \hat{\mathbf{Q}}}{\partial t} + \frac{\partial \hat{\mathbf{E}}}{\partial \xi} + \frac{\partial \hat{\mathbf{F}}}{\partial \eta} + J\frac{\partial \mathbf{G}}{\partial z} = \frac{\partial \hat{\mathbf{E}}_{\mathbf{v}}}{\partial \xi} + \frac{\partial \hat{\mathbf{F}}_{\mathbf{v}}}{\partial \eta} + J\frac{\partial \mathbf{G}_v}{\partial z}, \tag{2.19}$$

where $\mathbf{Q}$ is the conservative variables vector, $\mathbf{E}, \mathbf{F}, \mathbf{G}$ are the inviscid flux vectors, and $\mathbf{E_v}, \mathbf{F_v}, \mathbf{G_v}$ are the viscous flux vectors:

$$\begin{aligned}
\mathbf{Q} &= [\rho, \rho u, \rho v, \rho w, \rho e]^T \\
\mathbf{E} &= [\rho u, \rho u^2 + p, \rho uv, \rho uw, (\rho e + p)u]^T \\
\mathbf{F} &= [\rho v, \rho uv, \rho v^2 + p, \rho vw, (\rho e + p)v]^T \\
\mathbf{G} &= [\rho w, \rho uw, \rho vw, \rho w^2 + p, (\rho e + p)w]^T \\
\mathbf{E_v} &= [0, \tau_{xx}, \tau_{xy}, \tau_{xz}, -q_x + u\tau_{xx} + v\tau_{xy} + w\tau_{xz}]^T \\
\mathbf{F_v} &= [0, \tau_{yx}, \tau_{yy}, \tau_{yz}, -q_y + u\tau_{yx} + v\tau_{yy} + w\tau_{yz}]^T \\
\mathbf{G_v} &= [0, \tau_{zx}, \tau_{zy}, \tau_{zz}, -q_z + u\tau_{zx} + v\tau_{zy} + w\tau_{zz}]^T
\end{aligned} \tag{2.20}$$

The hats in Eq. (2.19) denote the transformation from the physical coordinates to the computational coordinates (the transformation of the viscous flux vectors is similar to the transformation of the inviscid flux vectors):

$$\hat{\mathbf{Q}} = J\mathbf{Q}, \qquad \hat{\mathbf{E}} = \frac{\partial y}{\partial \eta}\mathbf{E} - \frac{\partial x}{\partial \eta}\mathbf{F}, \qquad \hat{\mathbf{F}} = -\frac{\partial y}{\partial \xi}\mathbf{E} + \frac{\partial x}{\partial \xi}\mathbf{F}, \tag{2.21}$$

where J is the Jacobian of the change of coordinates:

$$J = \frac{\partial x}{\partial \xi}\frac{\partial y}{\partial \eta} - \frac{\partial x}{\partial \eta}\frac{\partial y}{\partial \xi}. \tag{2.22}$$

In HiPSTAR, a finite difference formulation of Eq. (2.19) is solved. Several different numerical methods are available in HiPSTAR, only the ones that are employed in the present study are mentioned in the following. Explicit fourth-order central differences are used for spatial discretisation, and a Carpenter boundary scheme [35] is employed to extend the fourth-order accuracy to the domain boundaries. A fourth-order low-storage Runge-Kutta scheme [36] is used for time integration. A nine-point, eighth-order standard filtering scheme [37] is used to enforce stability, and a skew-symmetric splitting formulation of the non-linear terms is used to reduce aliasing [38]. For an in-depth description of the numerical methods implemented in HiPSTAR, one can refer to Jones [39]. For the present study, HiPSTAR has been extended with an implementation of an overset grid method, as described in the next chapter.

Chapter 3

Overset grid method

3.1 Motivation

When dealing with complex geometries using finite difference methods on structured grids, it is almost unavoidable to use a multi-block setup. Particular attention must then be paid to the treatment of the interfaces between the different blocks, especially if accurate acoustic predictions are desired.

The simplest interface treatment is halo exchange: at interfaces the grid of each block is extended with halo regions where the solution obtained in the adjacent block is copied, so that the same finite difference scheme as used for the interior points can be applied at the interface. In consequence, no additional numerical error is generated at the interface, and the grid is subjected to the same constraint across the interface than inside the block, i.e. the grid cannot be singular across the interface (the metrics cannot be discontinuous). While this method would give the best accuracy, the constraint on the grid makes this method only suited to simple geometries.

In order to increase the flexibility of finite difference solvers using multi-block structured grids, Kim and Lee [40] developed the 'characteristic interface condition'. In this approach, one-sided finite difference schemes are employed for the near-interface points on each side of the interface, so that the differencing stencils do not cross the interface. The characteristics of the NSE are computed across the interface, and communicated from one block to the other according to their physical direction of propagation. As the differencing stencils do not cross the interface, the grid is allowed to be singular across the interface, this method only requires the interface points where the two blocks overlap. Despite its flexibility, the characteristic interface condition is subjected to some limitations:

- Where the component of the convection velocity normal to the interface is arbitrarily small (which happens either if the flow velocity is close to zero or if the velocity is aligned with the interface), the accuracy of the interface condition decreases significantly, sometimes even leading to instability.
- It has been observed that the abrupt change in the finite difference scheme can generate spurious acoustic waves when under-resolved hydrodynamic fluctuations cross the

interface.

- The interface points must match exactly in the two adjacent blocks, resulting in sub-optimal grid quality in some parts of the domain.

An alternative to the characteristic interface condition are the overset grid methods. The overset grid methods can be seen as generalisations of the halo exchange, which eliminate the requirement to exactly match the grid of the halo region of one block to the near boundary grid of the adjacent block. Instead, in the overset grid approaches the domain is divided in multiple structured grids that are completely independent of each other, and that overlap close to their boundaries. Next to the interfaces, rather than simply copying the solution between two matching points from different grids, an interpolation scheme is used to make the link between the overlapping regions of the overlapping grids (in case the points of the overlapping regions of two blocks match exactly, the interpolation simply becomes a copy of the solution between the matching points, so that the overset grid method naturally converges to a halo exchange). A specific algorithm is used for the generation of the composite mask in order to identify the discretisation, interpolation and exterior points, so that the same finite difference scheme can be used for all interior points [41], as for halo exchange. An example of an overset grid setup for the simulation of aerofoil flow is illustrated in Fig. 3.1.

To the author's knowledge, the application of overset grid methods to CFD simulation started in 1970 with an investigation of the inviscid transonic flow over aerofoils by Magnus and Yoshihara [42]. The method has then been further developed in the following years [43–45]. More recently, overset grid methods have been successfully used by different authors to handle aeroacoustics simulations of complex geometries with high-order finite difference methods [19, 46–48]. The main advantage of overset grid methods lies in their ability to provide great flexibility on the grid topology, especially as it allows to cut holes in a grid [46], while at the same time maintaining the accuracy of the simulation by using high-order interpolation [49]. This flexibility makes it possible to have nearly optimal grid quality in different regions of the domain dominated by different physics. This is particularly attractive for computational aeroacoustics: close to solid surfaces, body-fitted grids are used to accurately resolve the hydrodynamics fluctuations, whereas a single Cartesian background grid is used where the flow is nearly uniform to accurately predict the acoustic waves propagation [47].

As the simple halo exchange and the characteristic interfaces were not found to be satisfactory for the configuration of the present study, it was decided to implement an overset grid method framework in HiPSTAR. The actual implementation of an overset grid method in a CFD code is not straightforward, and some points require particular attention in order to produce accurate results, while keeping the computational cost to a minimum. In general, two additional pre-processing steps are required:

- The generation of the composite grid.

- The computation of the interpolation weights.

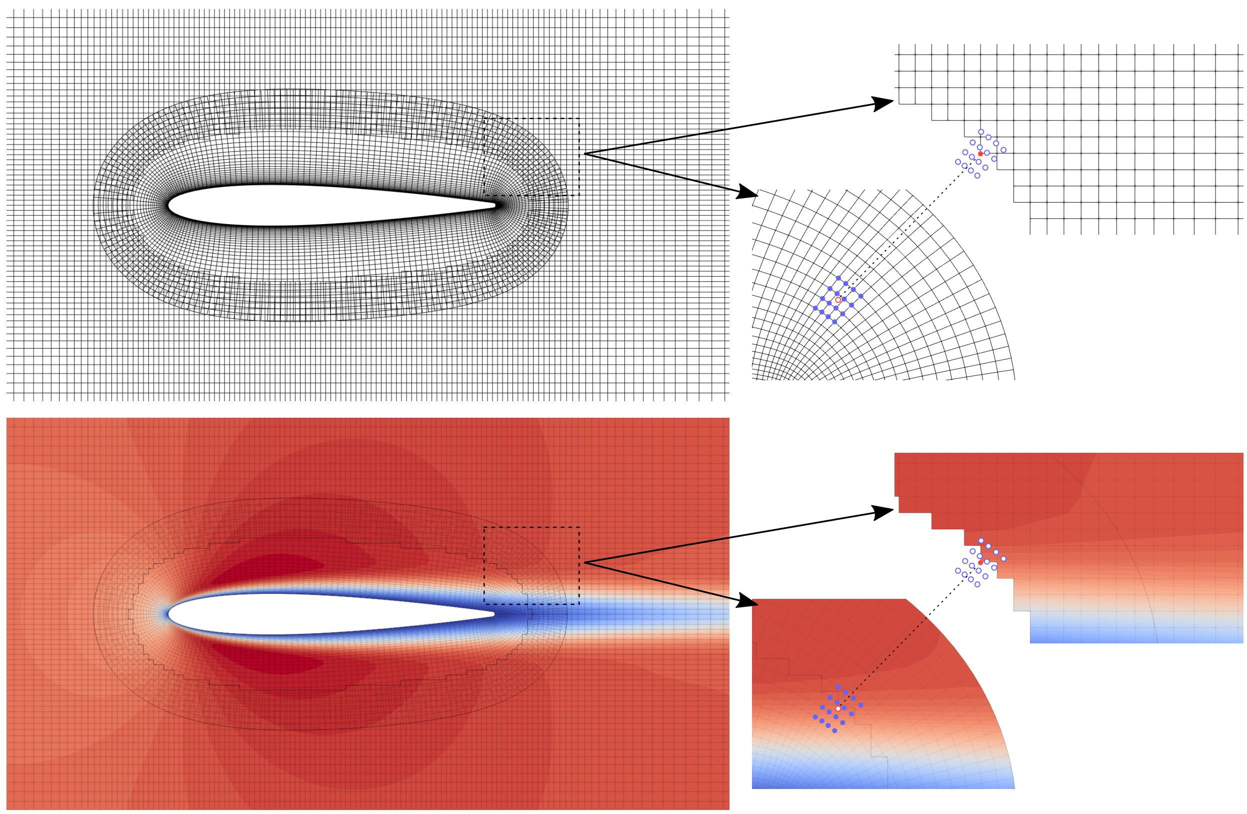

Figure 3.1: Example of a two blocks overset grid setup for the simulation of the flow around a NACA0012 aerofoil. The composite grid is presented on the top, with a close-up view of the overlapping region an interpolation stencil in the O-grid of a point of the background grid. The streamwise velocity after a few time-steps is shown on the bottom.

This newly implemented overset grid framework has already successfully been used for different simulations of the flow around aerofoils, and the resulting self-noise [50, 51]. The method, briefly presented in Deuse and Sandberg [50], is now described in further detail.

3.2 Implementation

3.2.1 Generation of the composite grid

The algorithm used to generate the composite grid is perhaps the most critical part of an overset grid method. It consists of the identification of the discretisation and interpolation points, and the hole cutting procedure [52]. Indeed, the quality of the composite grid has a major impact on the accuracy and the stability of the method. This part is also the most complicated to implement in a CFD code. There exist several codes that are able to produce composite grids [53–57], however it has been decided to implement a new dedicated algorithm, fully integrated in HiPSTAR in order to reduce and simplify the user input.

The procedure implemented in HiPSTAR was inspired by the algorithm of Chesshire and Henshaw [58]. With the current implementation, the three-dimensional domain is supposed to be uniform in the third dimension, so that the composite grid is actually two-dimensional. Nonetheless, the extension to full three-dimensional grids should not introduce additional difficulties. Similarly to the method of Chesshire and Henshaw [58], the composite grid generated will depend on the stencil size of the discretisation and interpolation schemes, and on the ordering of the grids. Based on a set of grids and their associated boundary conditions, each point is given a status:

- Discretisation point: nothing special needs to be done at this point, the same finite difference scheme applies as if no overset grid method was used.
- Interpolation point: the flow variables at this points are interpolated from their value in another block.
- Non-physical point: this point is not part of the computation, either because a hole has been cut in the grid at this location, or because the solution at this location will be computed in a different overlapping block.

Let N_B be the number of blocks in the computational setup. Each block b^k is given an index $k \in [1, ..., N_b]$ and is composed of a set of points $p^k_{i,j}$ where i and j are the indexes of the points in the structured grid (the third index is omitted as the domain is uniform in the third direction). Similarly to the algorithm of Chesshire and Henshaw [58], the objective of the composite grid generation procedure is to associate to each block b^k a flag array $F^k_{i,j}$ such that:

$$F^k_{i,j} = \begin{cases} k & \text{if } p^k_{i,j} \text{ is a discretisation point in } b^k. \\ -k' & \text{if } p^k_{i,j} \text{ is interpolated from } b^{k'}\text{, where } k \neq k'. \\ 0 & \text{if } p^k_{i,j} \text{ is a non-physical point.} \end{cases}$$

In order to construct these flag arrays, two additional sets of arrays of logicals $P^k_{i,j}$ and $S^{k,k'}_{i,j}$ are constructed in parallel to the flag arrays. The arrays $P^k_{i,j}$ will be such that $P^k_{i,j}$ is *false* only if $p^k_{i,j}$ is a non-physical point, and *true* otherwise. The arrays $S^{k,k'}_{i,j}$ are arrays of 'statuses' and will be such that:

- If $k = k'$, $S^{k,k'}_{i,j} = \mathit{true}$ only if $p^k_{i,j}$ is a valid discretisation point in b^k.
- If $k \neq k'$, $S^{k,k'}_{i,j} = \mathit{true}$ only if $p^k_{i,j}$ is a valid interpolation point from $b^{k'}$ into b^k.

A valid discretisation point (resp. interpolation point) is defined as a point that has no non-physical points in its finite difference stencil (resp. interpolation stencil). In HiPSTAR, a fourth-order central finite difference scheme is used, so that the finite difference stencil of $p^k_{i,j}$ is $\{p^k_{i+\Delta i,j}; \Delta i = -2, ..., 2\} \cup \{p^k_{i,j+\Delta j}; \Delta j = -2, ..., 2\}$. It has been decided to use an explicit fourth-order Lagrange interpolation scheme for the overset grid method, so that the interpolation stencil of $p^k_{i,j}$ from b^k into $b^{k'}$ is $\{p^{k'}_{i'+\Delta i,j'+\Delta j}; \Delta i = -2, ..., 2; \Delta j = -2, ..., 2\}$, where i' and j' are such that the distance between $p^{k'}_{i',j'}$ and $p^k_{i,j}$ is minimum.

The composite grid generation procedure is divided into multiple steps that are now detailed.

Step 1: At the beginning, all the $P^k_{i,j}$ arrays are set to *true*. Those arrays are then initialised similarly to the algorithm of Chesshire and Henshaw [58]: all the points that are the nearest to a point where a boundary condition is applied in another block are marked as non-physical:

Algorithm 1 Step 1

```
for k = 1, ..., N_b do
    for all p^k_{i,j} in b^k where a BC applies do
        for k' = 1, ..., N_b if k' ≠ k do
            Find i', j' that minimize the distance between p^{k'}_{i',j'} and p^k_{i,j}
            P^{k'}_{i',j'} ← false
        end for
    end for
end for
```

The purpose of this initialisation is to identify a first set of non-physical points. As reported by Chesshire and Henshaw [58], this step will not find all non-physical points, but the set of non-physical point will be expanded in the next step to fill out the exterior regions.

Step 2: The status of each point in the grid is computed iteratively. This part of the procedure is repeated until convergence is reached, i.e. until the arrays $S^{k,k'}_{i,j}$ and $P^k_{i,j}$ remain unchanged. This step is divided into two sub-steps:

Algorithm 2 Step 2

```
repeat
    has_changed ← false
    Step 2.1
    Step 2.2
until has_changed = false
```

Step 2.1: First, the arrays $S_{i,j}^{k,k'}$ are updated to reflect the statuses of all points in the grid (and track is kept of whether or not those arrays have been modified in the present iteration):

Algorithm 3 Step 2.1

```
for k = 1, ..., N_b do
    for all p^k_{i,j} in b^k do
        for k' = 1, ..., N_b do
            if k = k' then
                if p^k_{i,j} is a valid discretisation point in b^k then
                    is_valid ← true
                else
                    is_valid ← false
                end if
            else if k ≠ k' then
                if p^k_{i,j} is a valid interpolation point from b^{k'} into b^k then
                    is_valid ← true
                else
                    is_valid ← false
                end if
            end if
            if S^{k,k'}_{i,j} ≠ is_valid then
                S^{k,k'}_{i,j} ← is_valid
                has_changed ← true
            end if
        end for
    end for
end for
```

Step 2.2: Next, the arrays $P_{i,j}^{k}$ are updated. All points that are not valid discretisation points and that cannot be interpolated from any other block are marked as non-physical:

Algorithm 4 Step 2.2

for $k = 1, ..., N_b$ **do**
  for all $p_{i,j}^k$ in b^k **do**
    if $S_{i,j}^{k,k'} = \mathit{false} \; \forall \, k' = 1, ..., N_b$ **then**
      $P_{i,j}^k \leftarrow \mathit{false}$
    end if
  end for
end for

If any of the arrays $S_{i,j}^{k,k'}$ or $P_{i,j}^k$ have been modified during this iteration, the present step is repeated.

Step 3: The overset grid method deals with multiple overlapping grids, and so there can be some locations in the domain associated to multiple points from different blocks at the same time. It is however unnecessary to solve the system of Partial Differential Equations (PDEs) multiple times for different points which correspond to the same location. In the present algorithm, when that situation is encountered, the point from the block with the highest index is prioritized over the points from the other blocks. Those latter are marked as unnecessary discretisation points by modifying the arrays of statuses as follows:

Algorithm 5 Step 3

for $k = 1, ..., N_b$ **do**
  for all $p_{i,j}^k$ in b^k **do**
    for $k' = k + 1, ..., N_b$ **do**
      if $S_{i,j}^{k,k'} = \mathit{true}$ **then**
        $S_{i,j}^{k,k} \leftarrow \mathit{false}$
        break
      end if
    end for
  end for
end for

This step tends to identify too many points as unnecessary discretisation points, and so in the next steps some of the points that have been identified as unnecessary discretisation points during this step will be classified back as discretisation points.

Step 4: At this point, the arrays $S_{i,j}^{k,k'}$ and $P_{i,j}^k$ have been filled. This step consists of constructing the flag arrays $F_{i,j}^k$, i.e. associate a unique flag to each point. This step operates from the block with the highest index to the block with the lowest index. Similarly to step 2, the procedure is repeated until convergence is reached, and is restarted from the block with the highest index if the status of at least one point has changed during the current iteration. After the flag array of the block being processed has been initialized with 0, this step is divided into two sub-steps:

Algorithm 6 Step 4:

```
repeat
    has_changed ← false
    for k = N_b, ..., 1 do
        for all p^k_{i,j} in b^k do
            F^k_{i,j} ← 0
        end for
        Step 4.1
        Step 4.2
        if has_changed = true then
            break
        end if
    end for
until has_changed = false
```

Step 4.1: So far, all the interpolation possibilities have been identified in the arrays of statuses. As the interpolation is an expensive operation, only the necessary interpolation points are now identified. An interpolation is necessary at all points that are part of the finite difference stencil of a necessary discretisation point, but that are invalid or unnecessary discretisation points themselves. The interpolation from the blocks with the highest indexes is prioritized. If a point that had been identified as unnecessary discretisation matches this criterion, and cannot be interpolated from a block with a higher index, first it is verified if that point is a valid discretisation point. If so, the status of the point is updated to classify it as a necessary discretisation point.

Algorithm 7 Step 4.1

---

for all $p_{i,j}^k$ in b^k, if $S_{i,j}^{k,k} = true$ **do**
    for all $p_{i',j'}^k$ in the finite difference stencil of $p_{i,j}^k$ **do**
        if $S_{i',j'}^{k,k} = false$ **then**
            for $k' = N_b, ..., 1$ **do**
                if $k = k'$ and $p_{i',j'}^k$ is a valid discretisation point **then**
                    $S_{i',j'}^{k,k} \leftarrow true$
                    break
                else if $k \neq k'$ and $S_{i',j'}^{k,k'} = true$ **then**
                    $F_{i',j'}^k \leftarrow -k'$
                    break
                end if
            end for
        end if
    end for
end for

Step 4.2: All the points that require interpolation have been identified. Thanks to the procedure that has been used to identified them, it is guaranteed that those are valid interpolation points, i.e. there are no non-physical points in their interpolation stencils. Yet, as explicit interpolation is used, one must still ensure that all the points of the interpolation stencils are discretisation points. The arrays of statuses are thus updated accordingly, and if the array of statuses of a block with a higher index than the block being dealt with is updated, then step 4 is restarted from the beginning.

Algorithm 8 Step 4.2

---

for all $p_{i,j}^k$ in b^k, if $F_{i,j}^k < 0$ **do**
    $k' \leftarrow -F_{i,j}^k$
    for all $p_{i',j'}^{k'}$ in the interpolation stencil of $p_{i,j}^k$ from $b^{k'}$ **do**
        if $S_{i',j'}^{k',k'} = false$ **then**
            $S_{i',j'}^{k',k'} \leftarrow true$
            if $k' > k$ **then**
                `has_changed` $\leftarrow true$
            end if
        end if
    end for
end for

Step 5: The last step simply consists of setting the flag of the discretisation points to the correct value (so far they are still associated with flag 0):

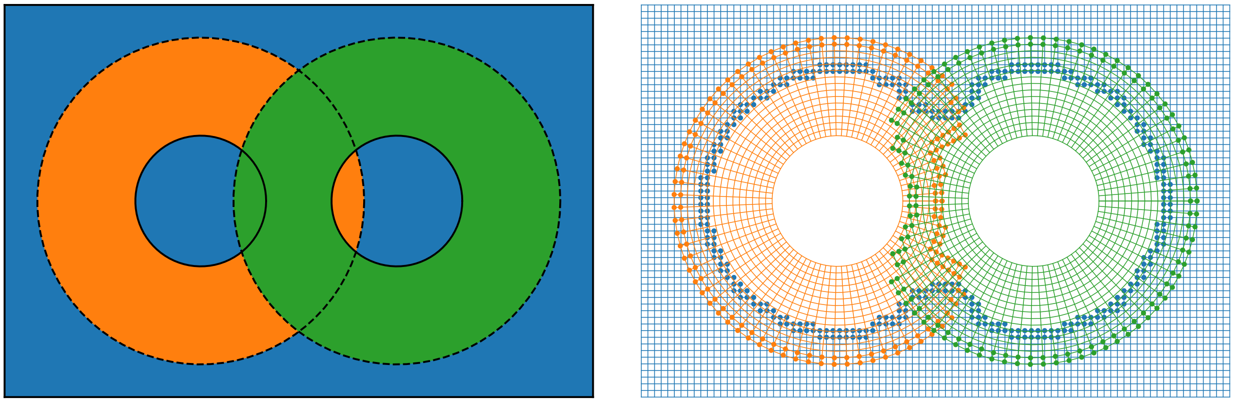

Figure 3.2: Example of a three block overset grid setup, for the simulation of the flow around two cylinders embedded in a rectangular box. The indexes of the blocks are $k = 1$ (blue), $k = 2$ (orange), $k = 3$ (green). The initial blocks are shown on the right, and the composite grid generated with HiPSTAR is shown on the left (the non-physical points are blanked, and the dots identify the interpolation points).

Algorithm 9 Step 5

for $k = 1, ..., N_b$ **do**
    for all $p^k_{i,j}$ in b^k **do**
        if $S^{k,k}_{i,j} = \textit{true}$ and $F^k_{i,j} = 0$ **then**
            $F^k_{i,j} \leftarrow k$
        end if
    end for
end for

An example of the composite mask generated with the algorithm presented above is shown in Fig. 3.2. As it can be seen, the algorithm is able to deal with multiple blocks with complex overlapping patterns, and produce an acceptable composite grid. As mentioned previously, discretisation points are prioritized in the block with the highest index whenever possible, and the number of interpolation points is minimum.

3.2.2 Computation of the interpolation weights

An explicit Lagrange interpolation scheme is used in the present overset grid method. Let us consider a function f of two variables ξ and η, discretised as $f_{ij} = f(\xi_i, \eta_j)$ where $\xi_i = i\Delta\xi$ and $\eta_j = j\Delta\eta$. In the present application, f denotes any flow variable, and ξ and η denote the computational coordinates in the block from which f is interpolated. The interpolated field $\tilde{f}$ is constructed as a linear combination of the discrete values f_{ij}, associated to the interpolation weights w_{ij}:

$$\tilde{f}(\xi, \eta) = \sum_{(i,j) \in \mathcal{S}} f_{ij} \, w_{ij} \, , \tag{3.1}$$

where $\mathcal{S}$ denotes the interpolation stencil. For Lagrange interpolation, the interpolation stencil is such that $\mathcal{S} = \mathcal{S}_\xi \times \mathcal{S}_\eta = \{i_1, ..., i_M\} \times \{j_1, ..., j_N\}$. As a fourth-order central finite difference scheme is used in HiPSTAR, a fourth-order Lagrange interpolation scheme is selected, with the aim of maintaining the formal order of accuracy of the solver. Consequently, the dimensions of the interpolation stencil are $M = N = 5$. The interpolation weights depend on ξ and η as follows:

$$w_{ij} = \prod_{k \in \mathcal{S}_\xi \, , \, k \neq i} \left(\frac{\xi - \xi_k}{\xi_i - \xi_k} \right) \prod_{l \in \mathcal{S}_\eta \, , \, l \neq j} \left(\frac{\eta - \eta_l}{\eta_j - \eta_l} \right) . \tag{3.2}$$

The interpolation is performed in computational space rather than in physical space, as it has been reported by Tam and Hu [41] to be more accurate. In order to interpolate a variable f at given location, the corresponding interpolation offsets ξ and η (in the block from which f is interpolated) are therefore needed. However, the interpolation points are only identified by their physical coordinates x and y. Thus the interpolation offsets need to be calculated, with the requirement that when the interpolation scheme is applied to the physical coordinates of the interpolation points themselves, those physical coordinates are mapped exactly. In other words, for an interpolation point with physical coordinates x and y, the interpolation offsets ξ and η must be such that:

$$\begin{cases} \tilde{x}(\xi, \eta) = x, \\ \tilde{y}(\xi, \eta) = y. \end{cases} \tag{3.3}$$

As suggested by Sherer and Scott [46], this problem can be solved iteratively using Newton's method:

$$\begin{bmatrix} \xi^{n+1} \\ \eta^{n+1} \end{bmatrix} = \begin{bmatrix} \xi^{n} \\ \eta^{n} \end{bmatrix} - J^{-1}(\xi^n, \eta^n) \cdot \left(\begin{bmatrix} \tilde{x}(\xi^n, \eta^n) \\ \tilde{y}(\xi^n, \eta^n) \end{bmatrix} - \begin{bmatrix} x \\ y \end{bmatrix} \right) , \tag{3.4}$$

where n is the index off the current iteration, and J is the Jacobian matrix, which can be easily computed thanks to the simple analytical formulation of the interpolation weights in case of the Lagrange interpolation method:

$$J = \begin{bmatrix} \partial_\xi \tilde{x} & \partial_\eta \tilde{x} \\ \partial_\xi \tilde{y} & \partial_\eta \tilde{y} \end{bmatrix} . \tag{3.5}$$

3.3 Improvement of the stability

It is well known that unless some sort of regularisation is employed (such as filtering [46] or artificial dissipation [41]), the overset grid methods are prone to numerical instabilities, especially when they are combined with low-dissipative, high-order methods [59–62]. In general, it cannot be guaranteed that the interpolation will not increase the energy of the solution, and so instabilities may arise next to overlapping interfaces. In its original version, the present overset grid method is not exempt of those stability issues: actually even with moderate filtering, some configurations can become unstable.

Filtering and/or numerical dissipation are not the only ways to address those stability issues. A different approach has been developed by Bodony et al. [59], based on the Simultaneous Approximation Term (SAT) methodology initially developed by Carpenter et al. [63]. In its original formulation, the SAT methodology is a procedure for imposing boundary conditions that solves a linear combination of the boundary conditions and the differential equation near the boundary, while enforcing the energy stability. Bodony et al. [59] adapted the SAT methodology to the overset grid method by closely tying the numerical discretisation of the spatial derivatives to the interpolation, and developed a provably stable overset grid method.

In the present study, another approach has been developed to improve the stability of the overset grid method. This approach is based on the understanding of how those instabilities arise. As reported by Sharan et al. [61], a common source of instability for overset methods are the numerical dispersive waves that get trapped in a subdomain due to repeated reflections between subdomain boundaries, and which may grow in time and eventually corrupt the entire solution field. This phenomenon is illustrated in Fig. 3.3 for a simple one-dimensional example of a perturbation travelling through a two-block overset grid setup:

(a) The perturbation travels in block 1 (blue) towards block 2 (red).

(b) The perturbation enters the interpolation region of block 2. It is interpolated from block 1 into block 2. Because the interpolation is not perfect, the perturbation injected in block 2 is not exactly identical to the one travelling in block 1 (the latter is unaffected by the interpolation).

(c) The perturbation travels in both blocks simultaneously. Because the discretisation is not identical in both blocks (i.e. different grids are used), the numerical dissipation and dispersion errors are different between the two blocks, and so the discrepancy between the two perturbations slightly increases here as well.

(d) The perturbation reaches the interpolation region of block 1. It is interpolated from block 2 into block 1, again with some interpolation error. The perturbation which was travelling in block 1 is thus overwritten with a slightly different solution in the interpolation region.

(e) The perturbation in block 2 remains unaffected by the interpolation, and continues to travel. In block 1, the mismatch between the travelling perturbation and the perturbation injected in the interpolation region results in a partial reflection of the perturbation. This reflection travels backward, and is only present in block 1.

(f) The reflected perturbation continues to travel in block 1. It is interpolated from block 1 into block 2 in the interpolation region.

(g) The primary reflection continues to travel in block 1. Similarly to (d), the mismatch of the solution in the interior of block 2 and in its interpolation region creates a secondary reflection, which travels forward in block 2. This secondary reflection is not present in block 1. At this point, the situation is identical to (e), and so successive reflections will keep getting generated.

This simple example illustrates how repeated reflections get trapped in the overlapping regions, where uncoupled numerical solutions coexist at the same location. The successive reflections generated by one isolated incoming perturbation could be progressively damped if some sort of filtering or artificial dissipation is used. However, this approach may fail if incoming perturbations are continuously sent towards the overlapping region. In this case, the two uncoupled solutions in the overlapping region might start to diverge, and render the whole simulation unstable.

Based on those observations, it appears that this kind of instability could be eliminated if one avoids having multiple uncoupled solutions in the overlapping regions. This can be realised by bringing the interpolation halos right next to each other. This approach is illustrated in Fig. 3.4, for the same case as Fig. 3.3:

(a) The perturbation travels in block 1 (blue) towards block 2 (red).

(b) The perturbation is interpolated from block 1 into block 2, with some interpolation error.

(c) The perturbation leaves the interpolation region of block 2, then it is immediately interpolated from block 2 into block 1, again with some interpolation error. There is thus a slight mismatch in block 1 between solutions on both sides of the limit of the interpolation region.

(d) The initial perturbation continues to travel in block 2. The mismatch in block 1 generates a small reflection which travels backwards.

(e) Both the initial and the reflected perturbation leave the interpolation region and continue to travel. There is no reflection trapped in the overlapping region, as there is no region where uncoupled solutions can coexist.

It appears from this example that although some numerical reflections might be generated at the overlapping interface, a clever design of the composite grid can prevent those to generate an instability. It is noted that the numerical reflections result from the interpolation error. If the interpolation error is zero, then there would not be any numerical reflection generated. This situation is encountered when the grids of the overlapping blocks match exactly in the interpolation regions (the overset grid method naturally converges to the simple halo exchange in this case).

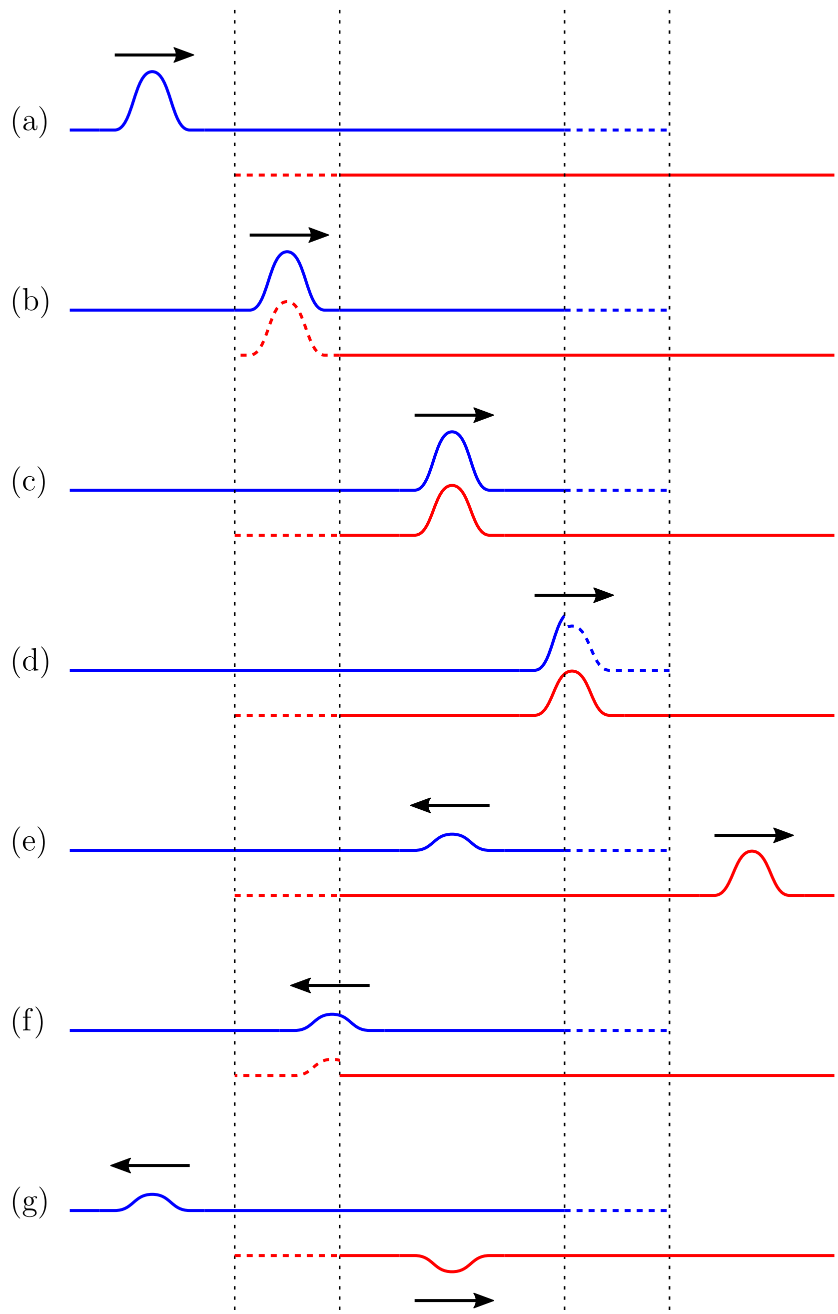

Figure 3.3: Example of a perturbation travelling through a one-dimensional two-block overset grid setup. The dotted lines identify the interpolation halos in both blocks. This setup includes a region where uncoupled solutions coexist at the same location.

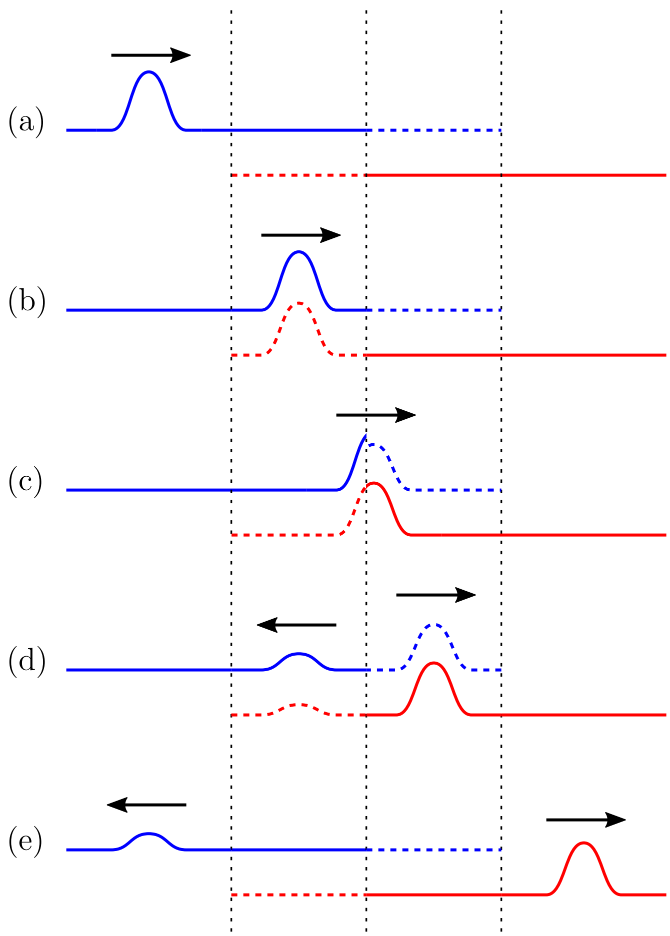

Figure 3.4: Example of a perturbation travelling through a one-dimensional two-block overset grid setup. The dotted lines identify the interpolation halos in both blocks. This setup has been designed such that there is no region where uncoupled solutions coexist at the same location.

To guarantee the stability of the method, one must then avoid having regions of the domain associated with discretisation points from multiple blocks. As it can be seen in Fig. 3.2, the composite grid generation algorithm presented above generates such regions. The proposed approach to improve the stability of the overset grid method is to bring the interpolation points from overlapping blocks closer to each other. One possible way would be to use decentred interpolation stencils, however this would be detrimental to the accuracy of the interpolation [46]. Another solution would be to use an implicit interpolation scheme, instead of an explicit interpolation scheme: this way an interpolation stencil of a given interpolation point could include some interpolation points of another block [58]. As the interpolation points are coupled, all the interpolations are computed at the same time by solving a linear system of equations. However, an implicit interpolation scheme is significantly more complicated to implement, and is more computationally expensive than an explicit scheme.

In order to solve the stability issue while avoiding the additional cost and complexity of implicit interpolation, a slightly modified version of the composite grid generation algorithm presented above has been developed. In this modified version, an interpolation stencil is allowed to contain other interpolation points, but only if those interpolation points are also valid discretisation points. In other words, a point can be both an interpolation and a discretisation point. At each time step during the simulation, firstly the solution field is updated at all discretisation points, then secondly the interpolation is performed at all interpolation points. At the mixed interpolation/discretisation points, the updated solution is simply overwritten with the interpolated solution, thus creating the coupling needed to render the method stable.

One-dimensional examples of composite grids are presented in Fig. 3.5. For the composite grid generated with the original version of the algorithm, the grey box highlights the region where two uncoupled solutions exist at the same location. As mentioned above, the implicit interpolation removes this issue, but has some disadvantages over explicit interpolation. The modified version of the algorithm successfully removes the region of uncoupled solutions, and only requires explicit interpolation. The price to pay is the increased number of interpolation points required (approximately doubled compared to the original version), however the cost penalty incurred is significantly lower than if an implicit interpolation was used.

In the modified version of the composite grid generation algorithm, step 4 of the original algorithm is modified, with an additional step 4.1.a right after step 4.1:

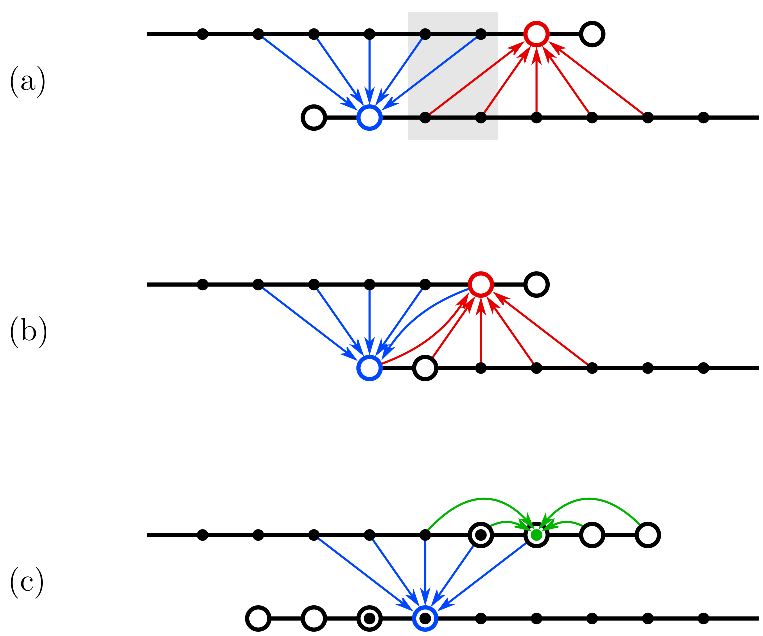

Figure 3.5: Examples of 1D composite grids. The solid dots identify the discretisation points and the hollow circles identify the interpolation points (for case (c), a point can be both). The blue and red arrows illustrate examples of interpolation stencils, the green arrows illustrate an example of a finite difference stencil. Case (a) corresponds to a composite grid generated with the original algorithm (the grey box identifies an area associated with discretisation points from both blocks), case (b) to a composite grid that would employ implicit interpolation, and case (c) to a composite grid generated with the modified algorithm.

Algorithm 10 Step 4 (modified)

```
repeat
    has_changed ← false
    for k = N_b, ..., 1 do
        for all p^k_{i,j} in b^k do
            F^k_{i,j} ← 0
        end for
        Step 4.1
        Step 4.1.a
        Step 4.2
        if has_changed = true then
            break
        end if
    end for
until has_changed = false
```

Step 4.1.a: In this sub-step, the mixed interpolation/discretisation points are identified. To do so, all the points that are part of the discretisation stencil of an interpolation point identified in step 4.1 are themselves turned into interpolation points (prioritizing the highest block) whenever possible. In order to differentiate the interpolation points identified in step 4.1 and step 4.1.a, a positive flag index is temporarily used in step 4.1.a, before correcting the sign of the flags once all the interpolation points have been identified.

Algorithm 11 Step 4.1.a

for all $p^k_{i,j}$ in b^k, if $S^{k,k}_{i,j} = true$ **do**
  for all $p^k_{i',j'}$ in the finite difference stencil of $p^k_{i,j}$ **do**
    if $F^k_{i',j'} < 0$ **then**
      for $k' = N_b, ..., 1$ **do**
        if $k = k'$ and $p^k_{i',j'}$ is a valid discretisation point **then**
          $S^{k,k}_{i',j'} \leftarrow true$
          break
        else if $k \neq k'$ and $S^{k,k'}_{i',j'} = true$ **then**
          $F^k_{i,j} \leftarrow k'$
          break
        end if
      end for
    end if
  end for
end for
for all $p^k_{i,j}$ in b^k **do**
  $F^k_{i,j} \leftarrow -|F^k_{i,j}|$
end for

A composite grid generated with the modified version of the algorithm is presented in Fig. 3.2. It can be seen that the modified version increases the number of interpolation points. Nonetheless, as it can be observed in Fig. 3.7 when only the interpolation and the non-physical points are blanked, the modified version of the algorithm successfully eliminates the issue of having multiple discretisation points associated to the same region of the domain. As a result, the slowly growing instability from the original version has not been observed with the modified version. Consequently, only the modified version is used in the rest of the present study.

3.4 Validation

3.4.1 Isentropic vortex test case

In order to validate the newly implemented overset grid method, two test cases have been selected. The first test case is the simulation of an isentropic vortex convected in a free-stream [64]. The governing equations are the compressible Euler equations (i.e. Re $\rightarrow \infty$ in the NSE), and the Mach number is M $= 0.4$. The two-dimensional computational domain consists of a square box of dimensions $[-30, 50] \times [-40, 40]$ in the x and y directions, with periodic boundary conditions at the outer boundaries. The vortex is initially located at $(x, y) = (0, 0)$, and is convected along the x direction over 20 non-dimensional time units, at the velocity $u_\infty = 1$. The initial flow field is:

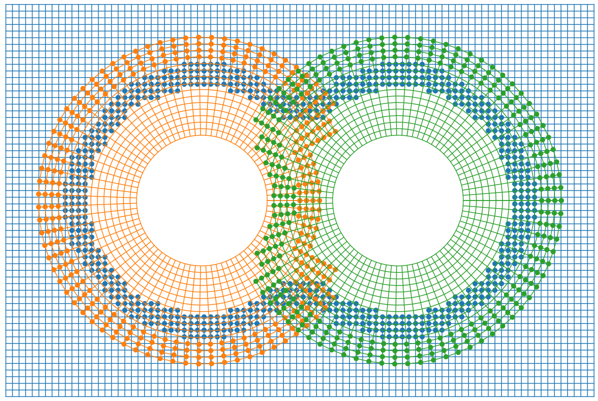

Figure 3.6: Composite grid generated with the modified version of the algorithm, for the same setup as Fig. 3.2.

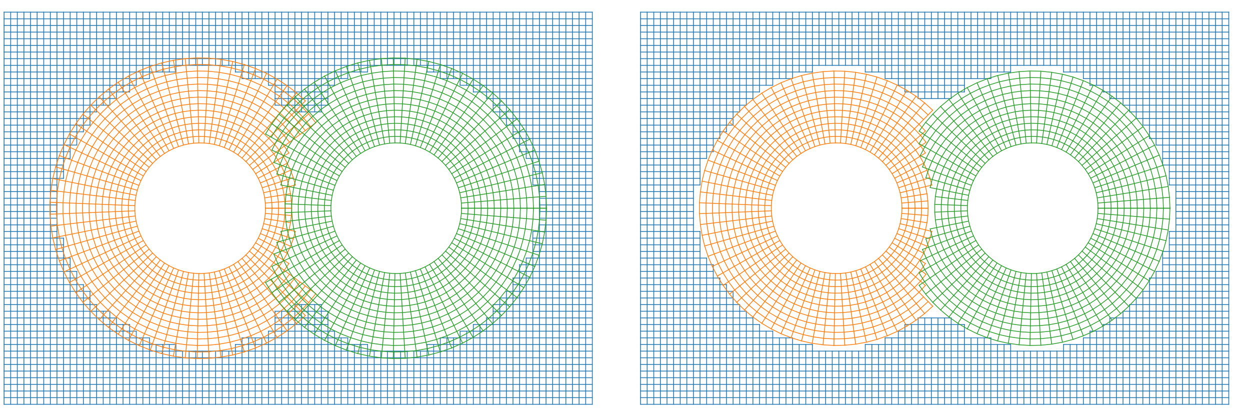

Figure 3.7: Comparison of the composite grid generated with the original version (left) and the modified version (right) of the algorithm. Only the discretisation points are shown, the interpolation and non-physical points are blanked.

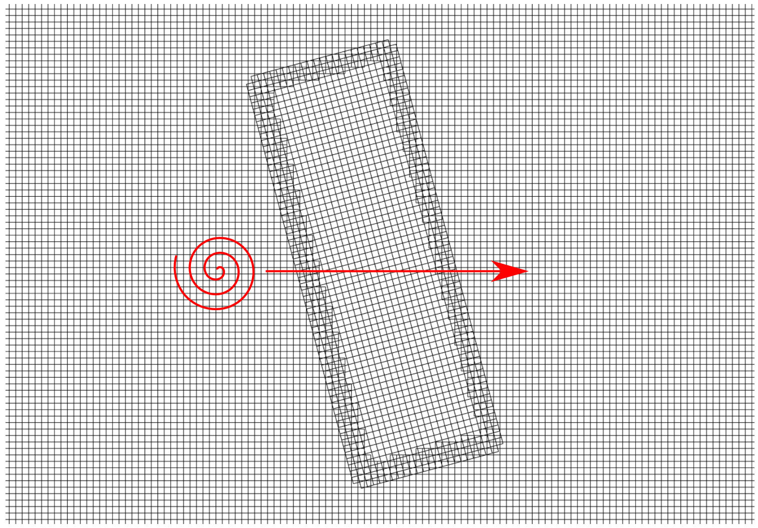

Figure 3.8: Grid topology of the two blocks setup for the isentropic vortex test case. As shown schematically in red, the vortex goes through the overlapping grid as it is convected in the domain.

$$
\begin{aligned}
u &= u_\infty - \alpha y e^{(1-r^2)/2} \\
v &= \alpha x e^{(1-r^2)/2} \\
w &= 0 \\
T &= 1 - \frac{1}{2}\alpha^2 M^2 (\gamma - 1) e^{1-r^2} \\
\rho &= \left[1 - \frac{1}{2}\alpha^2 M^2 (\gamma - 1) e^{1-r^2}\right]^{1/(\gamma-1)}
\end{aligned}
\tag{3.6}
$$

where α is the amplitude of the vortex ($\alpha = 0.1$ in the present study), and $r^2 = x^2 + y^2$. This test case is particularly useful as it admits an analytical solution to the compressible Euler equations: the vortex is simply convected along the streamwise direction.

Two grid configurations are compared, with various grid resolutions. The first grid configuration is a single block setup, covering the whole domain, and consisting of a single Cartesian grid with a uniform cell size, identical along the x and y directions. For the second grid configuration, a second Cartesian grid is superimposed to the aforementioned grid. This second grid is centred on the middle point of the domain, its dimensions are 10×26.66, and it is rotated around its centre of an angle of $\pi/12$. The cell size is identical in both grids. The two blocks are connected with the overset grid method. The vortex is initially located in the background grid; as it is convected through the flow, it goes through the superimposed grid, then back to the background grid. This setup is presented in Fig. 3.8.

After running the simulation for 20 non-dimensional time units, the simulated streamwise velocity u and density ρ are compared to their theoretical values u_{th} and ρ_{th} (i.e. simple

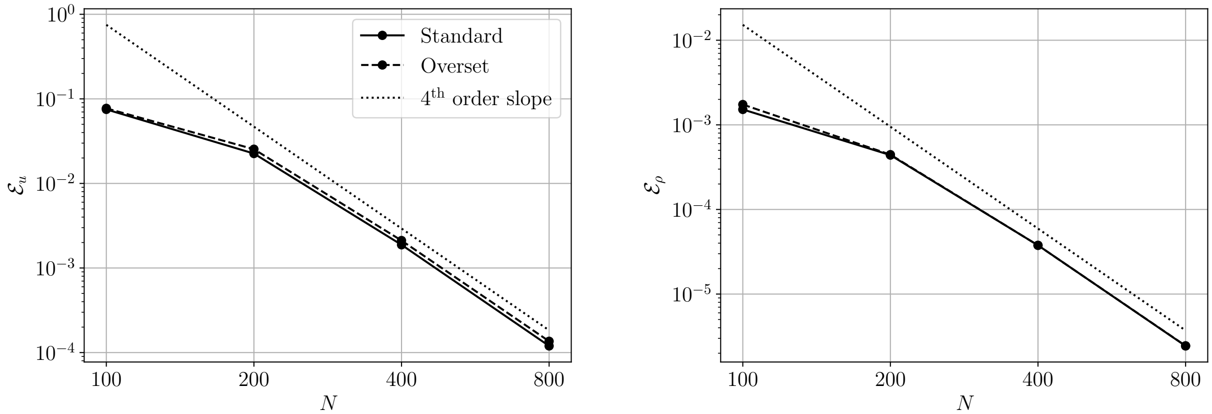

Figure 3.9: Evolution of the error metrics $\mathcal{E}_u$ (left) and $\mathcal{E}_\rho$ (right) in function of the number of points along the side of the domain. The single block setup (solid lines) and the two blocks setup (dashed lines) are compared.

convection of the vortex). Those value are integrated in a box Ω of size 8×8, centred on the final location of the vortex, in order to define the error metrics $\mathcal{E}_u$ and $\mathcal{E}_\rho$ as follows:

$$\mathcal{E}_u = \sqrt{\iint_\Omega (u - u_{\mathrm{th}})^2 \,\mathrm{d}x\,\mathrm{d}y}, \qquad \mathcal{E}_\rho = \sqrt{\iint_\Omega (\rho - \rho_{\mathrm{th}})^2 \,\mathrm{d}x\,\mathrm{d}y}. \tag{3.7}$$

Those error metrics are presented in Fig. 3.9 for the two grid setup; different grid resolutions, obtained by varying the number of points along the side of the domain (denoted N in Fig. 3.9), are compared. For a given grid resolution, the error metrics are almost identical for both grid setups, which indicates that the overset grid method does not introduce a significant additional numerical error. Moreover, it is observed that the order of accuracy of the solver remains unchanged when the overset grid method is applied.

3.4.2 Taylor-Green vortex test case

The Taylor-Green vortex flow [65] has been selected to rigorously validate the newly implemented overset grid method. In order to compare to the literature, the same setup as reported in DeBonis [66] is used (Re = 1600 and M = 0.1). The domain consists of a cube with sides of length 2π with periodic boundary conditions in each direction, and the initial condition is:

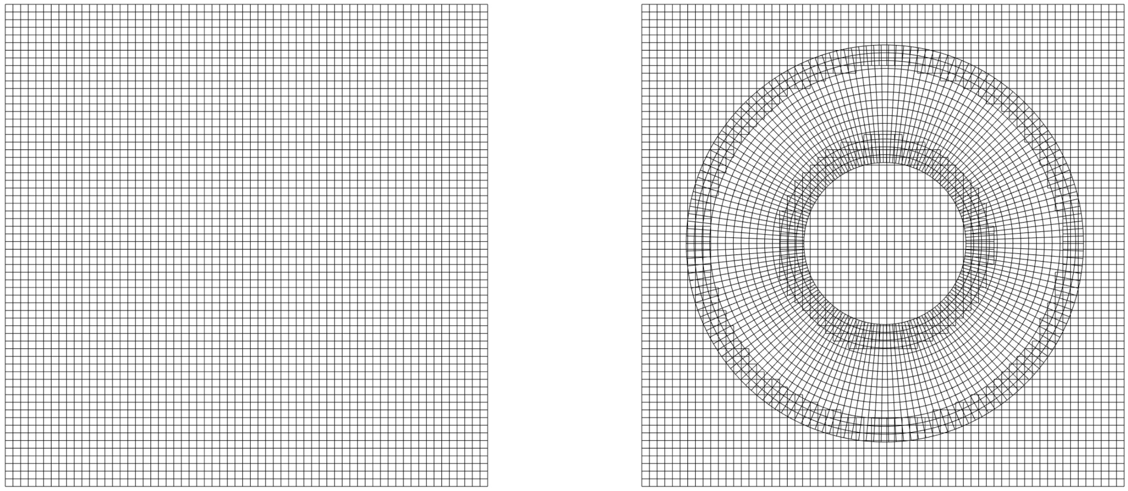

Figure 3.10: Span-normal view of the grid topology for the Taylor-Green vortex test case, for the single block case (left) and for the two-block case (right).

$$
\begin{aligned}
u &= \sin(x)\cos(y)\cos(z) \\
v &= -\cos(x)\sin(y)\cos(z) \\
w &= 0 \\
p &= \frac{1}{16\gamma \mathrm{M}^2}(\cos(2x)+\cos(2y))(\cos(2z)+2) \\
\rho &= 1.
\end{aligned}
\tag{3.8}
$$

Starting from this initial condition, the flow is then simulated for 20 time units. This flow displays a transient evolution implying turbulent transition, turbulence decay and complex vortex dynamics, and so it is a rigorous test case to validate CFD methods.

A single square block configuration has been compared to a two-block configuration, where the newly implemented overset grid method is used to overlap a hollow circular block to the square background as shown in Fig. 3.10. DNS were run for both setups. The grid resolution has been selected such that the largest cells of the circular grid have the same dimension as the cells of the square grid. Three grid resolutions have been tested: 64^3, 128^3 and 256^3 points in the square grid. Coarse grids have intentionally been used in order to assess the accuracy of the method when the flow structures are slightly under-resolved.

As reported by DeBonis [66], the primary method for evaluating the Taylor-Green vortex solutions is to examine the integrated kinetic energy in the domain E_k and its dissipation rate $-\mathrm{d}E_k/\mathrm{d}t$, where:

$$
E_k = \int_0^{2\pi}\int_0^{2\pi}\int_0^{2\pi} \rho \frac{u_i u_i}{2}\,\mathrm{d}x\,\mathrm{d}y\,\mathrm{d}z. \tag{3.9}
$$

The computed kinetic energy and its dissipation rate are presented in Fig. 3.11. For

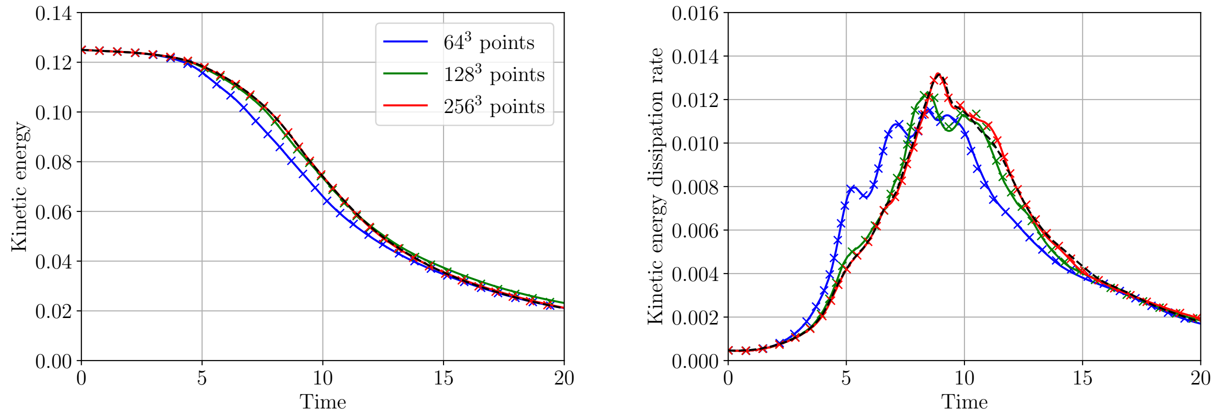

Figure 3.11: Kinetic energy (left) and its dissipation rate (right) of the Taylor-Green vortex, obtained with different grid resolutions. The solid lines correspond to the single block case and the crosses correspond to the two-blocks case with overset grid. The dashed black lines are the results of Jammy et al. [67] with a resolution of 256^3.

identical grid resolution, negligible differences are observed between the results of the single block case and the two-blocks case with overset grid, demonstrating that the present implementation of the overset grid method preserves the accuracy of HiPSTAR. Moreover, the finest grid resolution (256^3 points in the square grid) is in very good agreement with the results of Jammy et al. [67] obtained with the OpenSBLI framework [68].

3.5 Summary

In order to increase the flexibility of the solver, and to be able to deal with complex geometries while maintaining a high accuracy, an overset grid method framework has been implemented in HiPSTAR. This framework employs a new composite grid generation algorithm (inspired from the algorithm of Chesshire and Henshaw [58]), and a fourth-order accurate explicit Lagrange interpolation scheme. Two test cases have been used as a validation: the convection of an isentropic vortex, and the Taylor-Green vortex. For both cases, it has been shown that the overset grid method does not significantly impact the accuracy of the solver. In the next chapter, this new overset grid method will be employed in order to perform DNCs of the self-noise of a CD aerofoil.

Chapter 4

Computational domain and discretisation

4.1 Computational setup

The computational domain is illustrated in Fig. 4.1: a CD aerofoil at 8° of incidence is embedded in a rectangular box centred on the aerofoil TE. The location of the TE is $(x, y) = (0, 0)$. The domain extends from -7 to 7 in both x and y direction (which according to Jones [39] is sufficient to correctly capture the potential flow). A uniform inflow is prescribed at the left boundary. Non-reflective boundary conditions are applied at each outer boundary: sponge layers [39] are used at the left, top and bottom boundaries and a zonal characteristic boundary condition [69] is applied at the right boundary. The aerofoil is modelled as an adiabatic no-slip wall. All simulations are three-dimensional, and the domain is periodic in the spanwise direction. The spanwise correlation of the pressure along the aerofoil surface, and of the velocity in the near wake, have been investigated with a preliminary LES with a large spanwise length, as detailed in Section 4.2. Following this preliminary study, a span of 0.3 chord length has been selected, as it was found to be sufficient to fit the largest spanwise structures and to avoid spurious correlation due to the periodic boundary condition.

The hyperbolic grid generation scheme of Chan and Steger [70] is used to generate a high-quality body-fitted O-grid around the aerofoil (maximum skewness around 0.05). Details about this method are provided in Section 4.3. In the TE region, the O-grid is connected to a second block which encompasses the wake of the aerofoil. Great care is taken to enforce the continuity of the metrics at the interface, so that halo exchange can be used for the communication between those two blocks. The motivation here is to ensure that the hydrodynamic fluctuations will not generate spurious acoustic waves due to imperfect numerical interface conditions. Finally, a stretched Cartesian grid is used for the background; it is connected to the two other blocks using the overset grid presented in the previous chapter. This grid topology is illustrated in Fig. 4.2.

For each LES, the grid resolution is such that $(\Delta x^+, \Delta y^+, \Delta z^+) < (30, 1, 14)$ along the aerofoil surface, which is sufficient for wall-resolved LES according to Scillitoe et al. [34].

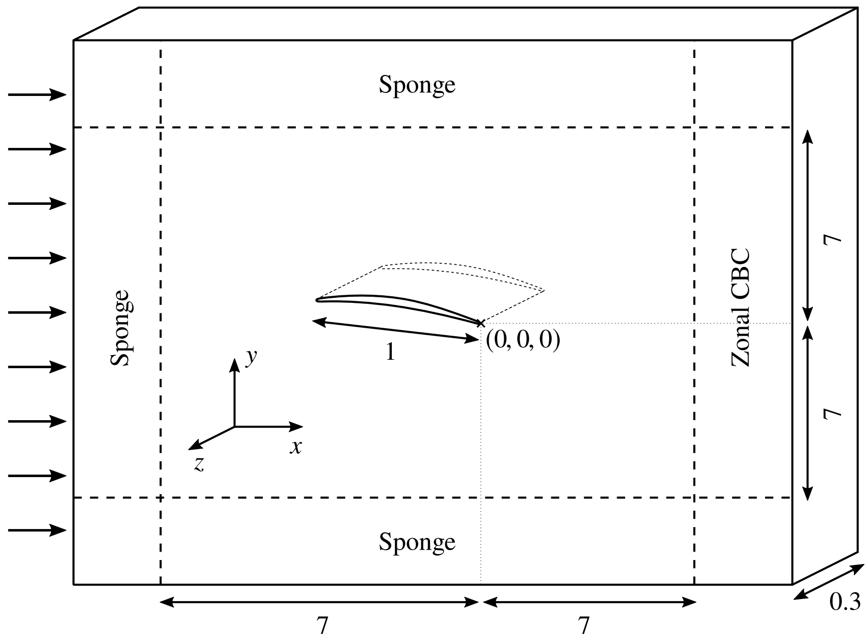

Figure 4.1: Schematic of the computational domain (not to scale).

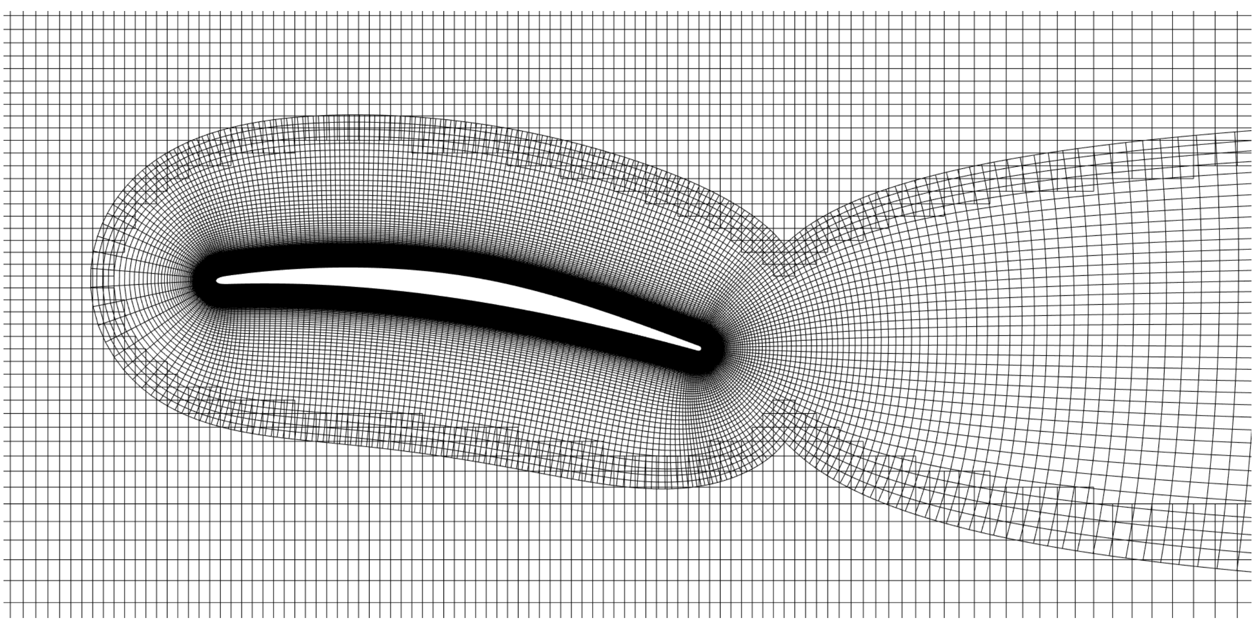

Figure 4.2: Grid close to the aerofoil for LES cases (only every 2nd point is shown).

For the DNS the grid resolution is such that $(\Delta x^+, \Delta y^+, \Delta z^+) < (8, 1, 8)$ along the aerofoil surface, similar to Wu et al. [23]. The grid resolution in the far-field is such that up to the frequency corresponding to the chord-based Strouhal number St = 2.5 the acoustic waves are discretised with at least 10 points per wavelength. For the DNS, a higher grid resolution is used in the region $x \in [-2.5, 1.5]$, $y \in [-1.5, 1.5]$, with at least 10 points per acoustic wavelength up to St = 38; the motivation is to properly resolve the acoustic waves coming from the LE separation bubble which were found to display a high frequency spectrum. The total number of points in the grid is about 46×10^6 for the LES and 402×10^6 for the DNS.

For all cases, the time step is selected as large as possible to minimise the computational cost while avoiding numerical instabilities. The Courant-Friedrichs-Lewy (CFL) number does not exceed 1.5 for the LES and 1.7 for the DNS. Even if the maximum value of the CFL number at some locations in the flow is slightly larger than unity, stable solution is obtained thanks to the skew-symmetric splitting formulation, the robustness of the 5-steps Runge-Kutta time stepping and the explicit filtering. Finally, for all cases the results of at least 12 non-dimensional time units were stored (after the initial transient had faded).

4.2 Selection of the spanwise extent of the domain

The spanwise extent of domain needs to be selected carefully in order to ensure that the periodicity of the spanwise direction does not affect the breakdown of the turbulent structures in the boundary layer and the wake. To do so, a first preliminary LES is conducted, using a relatively large span length of $L_z = 0.4$ chord lengths. The time evolution of the pressure along the aerofoil upper surface and of the streamwise velocity in the wake are saved, and spanwise correlations are computed. The (normalised) spanwise correlation $\gamma_{aa}(\Delta z)$ of a given variable $a(z)$ is defined as:

$$\gamma_{aa}(\Delta z) = \frac{\displaystyle\int_0^{L_z} a'(z + \Delta z) a'(z) \mathrm{d}z}{\displaystyle\int_0^{L_z} {a'}^2(z) \mathrm{d}z}\,, \tag{4.1}$$

where:

$$a'(z) = a(z) - \int_0^{L_z} a(Z) \mathrm{d}Z. \tag{4.2}$$

The normalised correlations for the case M = 0.4 are presented in Figs. 4.4 and 4.5. For this case, the main peaks in the correlation curves are comprised in $-0.05 < \Delta z < 0.05$, with significant negative correlation up to $-0.1 < \Delta z < 0.1$ in the wake. Therefore, for this case it appears that a spanwise length of 0.3 chord lengths ($-0.15 < \Delta z < 0.15$) is sufficient to eliminate the issue of the spanwise coherence.

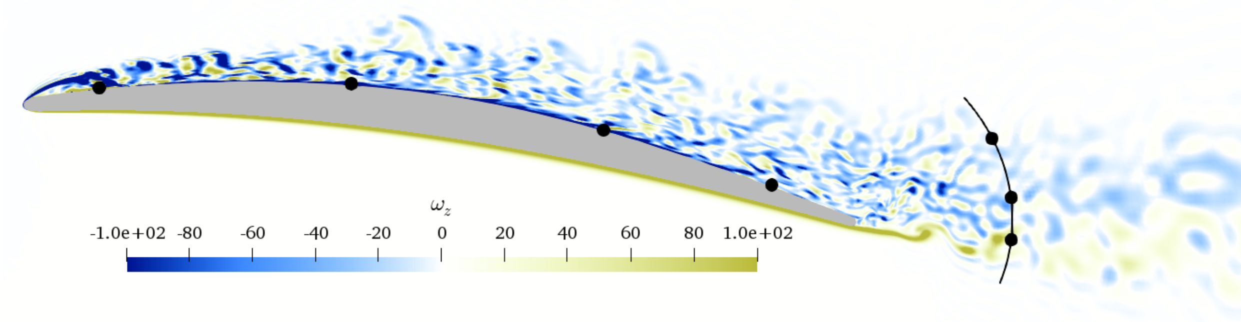

Figure 4.3: Instantaneous spanwise vorticity field, the black dots indicate the locations for the curves in Figs. 4.4 and 4.5.

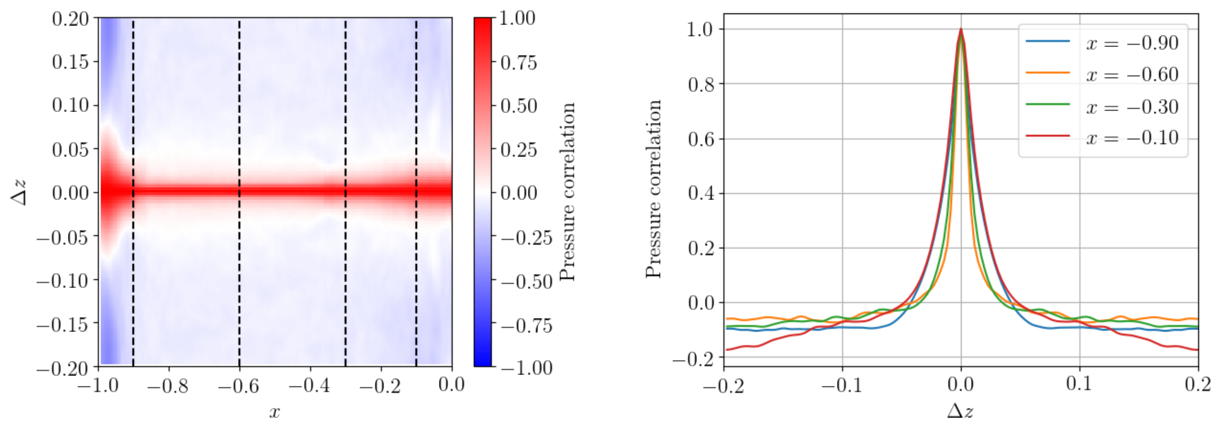

Figure 4.4: Spanwise correlation (normalised) of the pressure along the aerofoil upper surface.

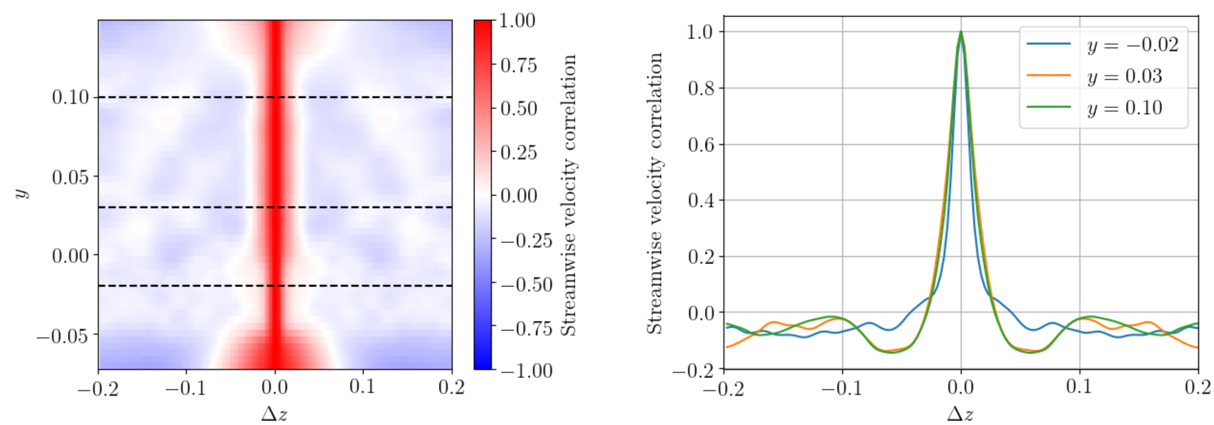

Figure 4.5: Spanwise correlation (normalised) of the streamwise velocity in the wake.

4.3 Hyperbolic grid generation method

The hyperbolic grid generation method is particularly well suited for the generation of high-quality structured grids for external aerodynamics. It is based on the resolution of a system of hyperbolic PDEs that enforce the grid orthogonality and cell size constraints [71]. In two-dimensions, those PDEs are solved in the computational space (ξ, η) and the resolution of those PDEs produces the mapping from the computational coordinates to the physical coordinates, i.e. the functions $x(\xi, \eta)$ and $y(\xi, \eta)$. The governing equations are (the subscripts ξ and η denoting the derivative with respect to the corresponding computational coordinate):

$$x_\xi x_\eta + y_\xi y_\eta = 0, \tag{4.3}$$

$$x_\xi y_\eta - y_\xi x_\eta = \Delta A. \tag{4.4}$$

The orthogonality between the lines of constant ξ and constant η is enforced by Eq. (4.3), while Eq. (4.4) allows to prescribe the local cell area ΔA. Those two PDEs are non-linear, therefore in order to solve them numerically they are linearised about a known state $\mathbf{r}^0 = [x_0, y_0]^T$, and the following system of linear PDEs is obtained:

$$\underbrace{\begin{bmatrix} x_\eta^0 & y_\eta^0 \\ y_\eta^0 & -x_\eta^0 \end{bmatrix}}_{\mathbf{A}} \underbrace{\begin{bmatrix} x_\xi \\ y_\xi \end{bmatrix}}_{\mathbf{r}_\xi} + \underbrace{\begin{bmatrix} x_\xi^0 & y_\xi^0 \\ -y_\xi^0 & x_\xi^0 \end{bmatrix}}_{\mathbf{B}} \underbrace{\begin{bmatrix} x_\eta \\ y_\eta \end{bmatrix}}_{\mathbf{r}_\eta} = \underbrace{\begin{bmatrix} 0 \\ \Delta A + \Delta A^0 \end{bmatrix}}_{\mathbf{f}}. \tag{4.5}$$

If $(x_\xi^0)^2 + (y_\xi^0)^2 \neq 0$, then the matrix $\mathbf{B}$ is invertible and the following equation is obtained:

$$\mathbf{r}_\eta = \mathbf{B}^{-1}\mathbf{f} - \mathbf{B}^{-1}\mathbf{A}\mathbf{r}_\xi. \tag{4.6}$$

The initial condition is expressed as $\mathbf{r}(\xi, \eta = 0)$ which corresponds to a given two-dimensional curve. In the context of external aerodynamics, the initial curve typically corresponds to the contour of an immersed body, and periodic boundary conditions are imposed in the ξ direction. Eq. (4.6) is solved with a finite difference method, by performing a marching in the η direction. At each step, the known state $\mathbf{r}^0$ is taken as the solution obtained at the previous step. Further details about this hyperbolic grid generation method can be found in Chan and Steger [70].

Chapter 5

Results and findings

5.1 Introduction

In the previous chapters, the methodology employed in the present study has been described. The motivation of the present study is to investigate the flow and the self-noise produced by an isolated aerofoil. To do so, DNC are conducted in order to obtained a detailed depiction of the turbulent flow, and how it leads to the production of noise. The CD aerofoil geometry is selected as this geometry is representative of low speed compressor blades. The Reynolds number is $\mathrm{Re} = 10^5$, and the angle of attack is $\alpha = 8°$ (this angle corresponds to the design condition for the CD aerofoil geometry [25]). In order to investigate the influence of the compressibility effects on the aerofoil self-noise, four different values of the free-stream Mach number are considered: $\mathrm{M} = [0.2, 0.3, 0.4, 0.5]$.

The HiPSTAR code, and the newly implemented overset grid framework described previously, are used to conduct LES of the four different cases. In order to validate those LES, and demonstrate the that this methodology is able to accurately simulate the turbulent structures and the noise sources, a DNS is also conducted for the case $\mathrm{M} = 0.4$. In the present chapter, the results of those numerical simulations are presented and analysed.

5.2 Hydrodynamic field

An instantaneous picture of the spanwise vorticity field ω_z is presented in Fig. 5.1, and the average pressure field and mean streamlines are presented in Fig. 5.2 for $\mathrm{M} = 0.4$ (for all the Mach numbers, the flow was found to be qualitatively similar). On the suction side, it is observed that the laminar flow separates right from the LE, then transitions to turbulence and reattaches in a highly time-dependent fashion. The flow then remains attached up to the TE, although it appears to be on the verge of separation in the second half of the upper surface. On the pressure side, it is observed that the flow remains laminar and fully attached up to the TE, then the shear layer separates, undergoes Kelvin-Helmholtz instability, and transitions to turbulence as it gets mixed with the turbulent flow coming from the suction side.

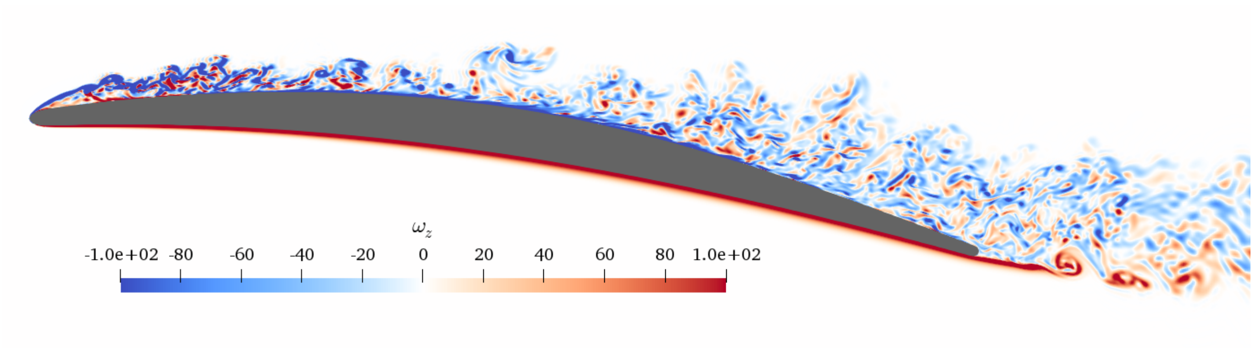

Figure 5.1: Instantaneous field of spanwise vorticity, M = 0.4, DNS results.

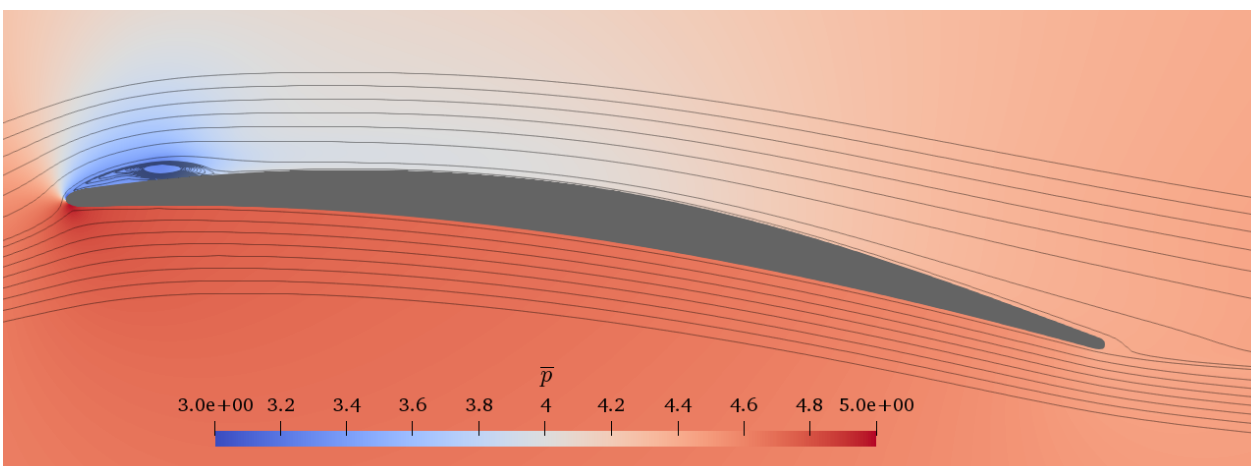

Figure 5.2: Average pressure field and mean streamlines, M = 0.4, DNS results.

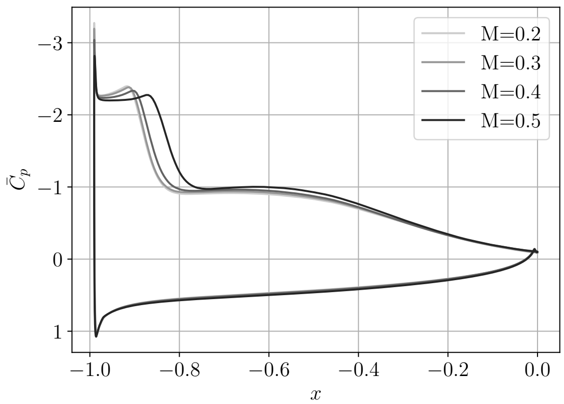

Figure 5.3: Average pressure coefficient, LES results.

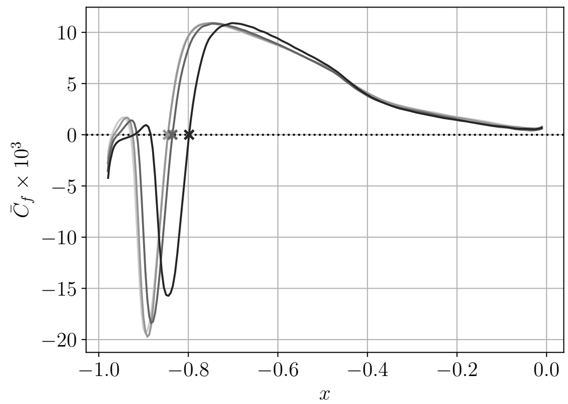

Figure 5.4: Average friction coefficient (upper surface only), LES results.

The distribution of the average pressure and friction coefficients along the aerofoil chord are presented in Figs. 5.3 and 5.4 respectively. Those coefficients are defined as $C_p = (p - p_0)/(\frac{1}{2}\rho_0 U_0^2)$ and $C_f = \tau_w/(\frac{1}{2}\rho_0 U_0^2)$ where τ_w denotes the wall shear stress, and the subscript 0 indicates the value in the free-stream. The whole pressure side is subjected to a favourable pressure gradient. On the suction side, the separation bubble creates a strong pressure drop close to the LE. Downstream of the separation bubble, the mean pressure is approximately constant up to mid-chord, then an adverse pressure gradient is observed up to the TE.

Next to the LE on the suction side, the friction coefficient is almost zero. Rapidly, the separation bubble creates a recirculation region which results in a region of negative C_f. The friction coefficient is then positive along the rest of the suction side. The location where the time averaged C_f reaches zero (identified by the crosses in Fig. 5.4) is considered as the end of the separation bubble, and the size of the separation bubble is defined as the distance between the LE and that location. The size of the separation bubble for the different Mach number cases is presented in Fig. 5.7 (solid line).

The curves of both C_p and C_f collapse almost exactly for the cases $\mathrm{M} = 0.2$ and $\mathrm{M} = 0.3$, indicating the independence of those coefficients to the Mach number in the low Mach number range. Differences emerge for $\mathrm{M} = 0.4$, and become larger for $\mathrm{M} = 0.5$. The main effect of the compressibility is to delay the reattachment region further downstream, and so to increase the size of the separation bubble when the Mach number is increased. It is not surprising to see the largest difference between the different cases in the LE region, as it is where the local Mach number is the largest. For free-stream Mach number $\mathrm{M} = [0.2, 0.3, 0.4, 0.5]$, the maximum value of the local Mach number is $\mathrm{M}_{\mathrm{max}}^{\mathrm{loc}} \approx [0.35, 0.55, 0.75, 1.0]$.

Similarly to Jones et al. [72], the Probability Density Functions (PDFs) of the friction coefficient for the four Mach numbers have been computed. Those are presented in Fig. 5.5. At any given location along the upper surface, the distributions of C_f appear to be Gaussian. For all the Mach numbers, it is observed that the variance has its maximum in the reat-

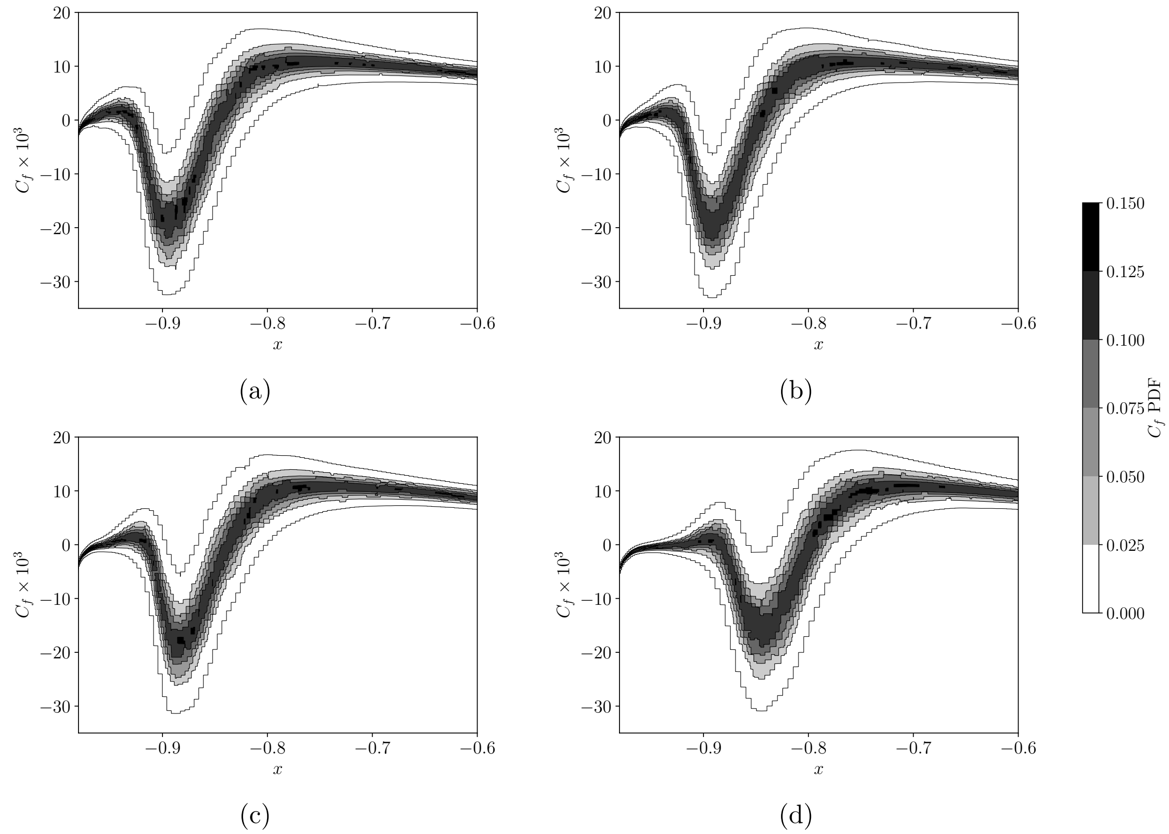

Figure 5.5: Iso-contours of the friction coefficient PDF close to the LE (upper surface only), LES results. The four Mach numbers are presented: M = 0.2 (a), 0.3 (b), 0.4 (c), 0.5 (d).

tachment region, indicating that the size of the separation bubble fluctuates significantly. The standard deviation of the friction coefficient $\sigma(C_f)$ is used to quantify the variance of the size of the separation bubble: as illustrated by the red segment in Fig. 5.6, the variance of the size of the separation bubble is defined as the distance between the locations where $\bar{C}_f + \sigma(C_f) = 0$ and $\bar{C}_f - \sigma(C_f) = 0$ next to the average reattachment point. It can be seen in Fig. 5.7 that although the Mach number significantly influences the average size of the separation bubble, it has little influence on its variance.

The lift coefficient C_l and the drag coefficient C_d are obtained by computing the integral of the pressure and friction coefficient along the aerofoil surface:

$$C_l = \int_S \left(C_f\,\vec{t} - C_p\,\vec{n}\right) \cdot \vec{e}_y \,\mathrm{d}S, \tag{5.1}$$

$$C_d = \int_S \left(C_f\,\vec{t} - C_p\,\vec{n}\right) \cdot \vec{e}_x \,\mathrm{d}S, \tag{5.2}$$

where $\vec{t}$ and $\vec{n}$ are respectively the local unit tangent and normal vectors, and $\vec{e}_x$ and $\vec{e}_y$ are the unit vectors pointing respectively in the streamwise and the vertical direction. The

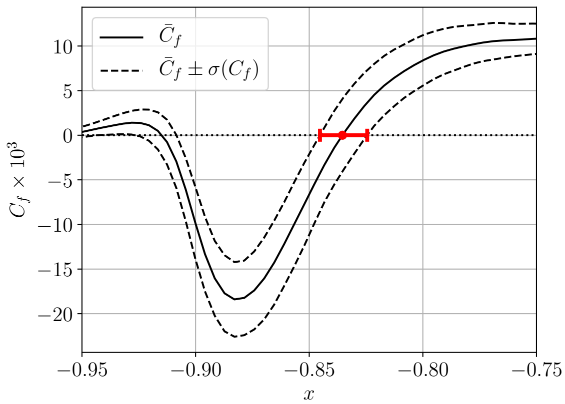

Figure 5.6: Average and standard deviation of the friction coefficient close to the LE, M = 0.4, LES results.

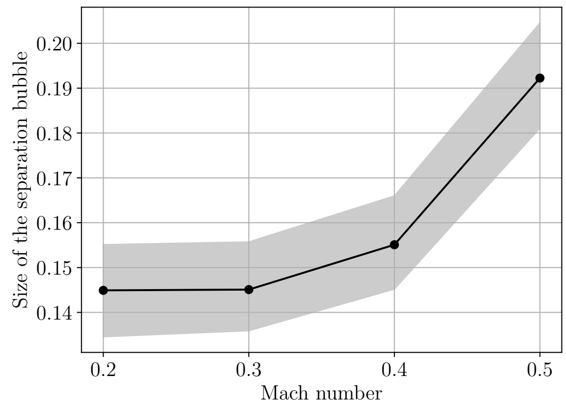

Figure 5.7: Size of the separation bubble in function of the Mach number (solid line) and its variance (grey region), LES results.

evolution of the time averaged lift and drag coefficients in function of the Mach number is presented in Fig. 5.8. The same behaviour is observed for both C_l and C_d, i.e. they increase with the Mach number: an increase of about 10% is observed between M = 0.2 and M = 0.5. This behaviour is not unexpected, as C_l and C_d should approximately scale as $1/\sqrt{1-\mathrm{M}^2}$ [73].

5.3 Boundary layer

The definition of boundary layer parameters involves reference values of the density and velocity. Consequently, the traditional definition of boundary layer parameters as used for flat plate boundary layers has to be adapted to be consistent with the spatially varying potential flow in the case of aerofoil flow. In the present study, the following definitions are used for the displacement thickness δ^* and the momentum thickness θ (where ξ and n denote respectively the tangential and the normal coordinate to the aerofoil surface):

$$\delta^*(\xi) = \int_0^\infty \left(1 - \frac{\rho(\xi,n)}{\rho_{\mathrm{is}}(\xi,n)} \frac{\upsilon(\xi,n)}{\upsilon_\infty(\xi)}\right) \mathrm{d}n, \tag{5.3}$$

$$\theta(\xi) = \int_0^\infty \frac{\rho(\xi,n)}{\rho_{\mathrm{is}}(\xi,n)} \frac{\upsilon(\xi,n)}{\upsilon_\infty(\xi)} \left(1 - \frac{\upsilon(\xi,n)}{\upsilon_\infty(\xi)}\right) \mathrm{d}n. \tag{5.4}$$

The new quantities υ and ρ_{is} have been constructed to address the issue of the spatially varying potential flow. The pseudo-velocity υ, as defined by Jones [39], is obtained by taking the integral of the spanwise vorticity in the wall normal direction:

$$\upsilon(\xi,n) = -\int_0^n \omega_z(\xi,\eta)\mathrm{d}\eta. \tag{5.5}$$

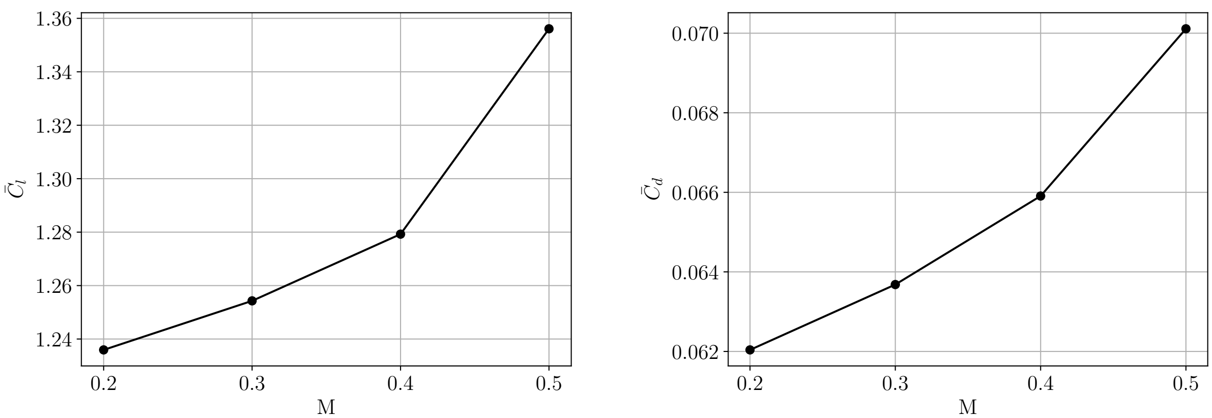

(a) (b)

Figure 5.8: Time averaged lift (a) and drag (b) coefficients in function of the Mach number, LES results.

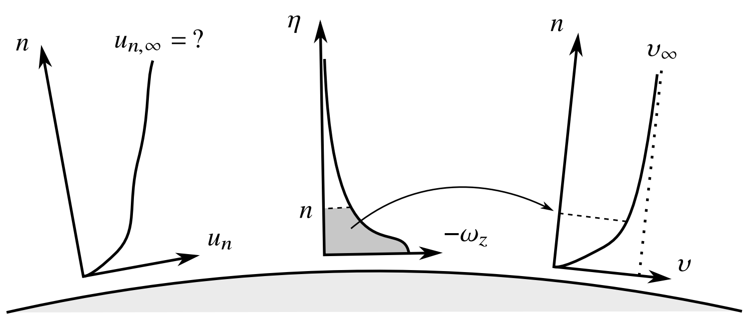

Figure 5.9: Schematic of the definition of the pseudo-velocity.

Close to the wall, it can be shown by substituting the definition of the vorticity in Eq. (5.5) that the pseudo-velocity converges to the tangential velocity. As the vorticity quickly reaches zero where the flow is inviscid, the pseudo-velocity is constant for sufficiently large values of n, and this constant value can be used as the reference velocity: $v_\infty(\xi) = v(\xi, n \to \infty)$. Fig. 5.9 illustrates the definition of the pseudo-velocity. A similar approach is developed for the reference density; an isentropic density has been defined as follows (the subscript 0 indicates the value in the free-stream):

$$\rho_{\text{is}}(\xi, n) = \rho_0 \left(\frac{p(\xi, n)}{p_0} \right)^{1/\gamma}. \tag{5.6}$$

In the (isentropic) potential flow, the relation $p/\rho^\gamma = p_0/\rho_0^\gamma$ holds, so that ρ_{is} is the actual density. As ρ_{is} is constructed solely from the pressure, its value is constant across the boundary layer in the wall normal direction, and this quantity is well suited as the reference density. Practically, it has been observed that the definitions of Eq. (5.4) are robust in the sense that they are fairly insensitive to the integration length in the normal direction, as long as it is large enough.

The boundary layer thicknesses δ^* and θ and the shape factor δ^*/θ along the aerofoil upper surface are presented in Fig. 5.10 for the different Mach numbers. Near the LE, the displacement thickness reaches a local maximum in the separation bubble while the momentum thickness is nearly zero, resulting in a very large shape factor. In the reattachment region, the shape factor drops abruptly, then close to the mid-chord where there is about zero pressure gradient, a plateau is observed at a value of about 1.6. Along the second half of the chord both the two thicknesses and the shape factor increase because of the adverse pressure gradient. Again, the results of the cases M = 0.2 and M = 0.3 collapse almost exactly. Differences rise starting from M = 0.4, as the curves of the boundary layer thicknesses are translated further downstream. A similar but more pronounced shift is observed for M = 0.5. This is consistent with the conclusion of the previous section: increasing the Mach number modifies the size of the separation bubble and moves the reattachment region further downstream.

Finally, the LES and DNS are in good agreement as shown in Fig. 5.11. Indeed, the LES are well resolved so that the average value of the ratio μ^{sgs}/μ does not exceed 0.5 close to the aerofoil surface, as shown in Fig. 5.12 for the case M = 0.4. Thus, this anchoring of the LES against a DNS gives confidence in using the LES approach for the parametric study.

5.4 Surface pressure spectrum

The surface pressure spectra at four different locations along the aerofoil upper surface are presented in Fig. 5.13. Note that in the following, each Power Spectral Density (PSD) is computed with Welch's method [74], using a segment size of 1/4 of the full signal length (12 time units), with 50% overlap between consecutive segments, and using a Hanning window. On the middle part of the upper surface ($x = -0.70$ and $x = -0.4$) all Mach number cases collapse quite well over almost the whole frequency range, whereas larger discrepancies are

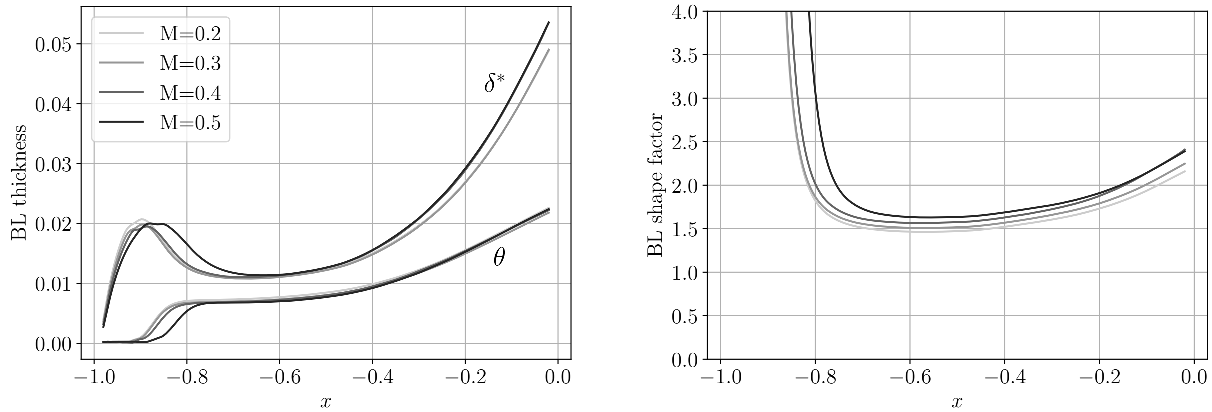

(a)

(b)

Figure 5.10: Boundary layer parameters along the aerofoil upper surface, LES results. Boundary layer displacement and momentum thicknesses (a), and shape factor (b).

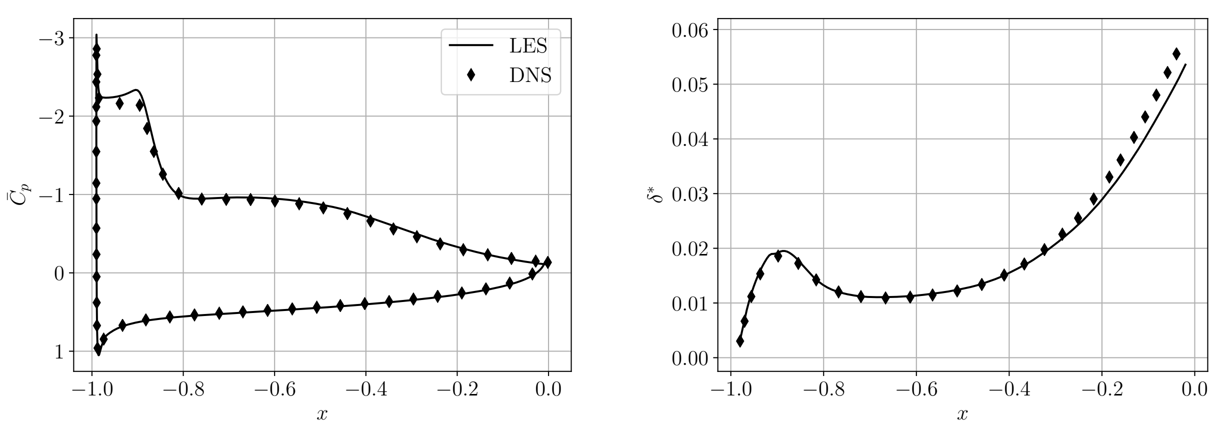

(a)

(b)

Figure 5.11: Comparison between LES and DNS results at M = 0.4 for the average pressure coefficient (a) and boundary layer displacement thickness along the upper surface (b).

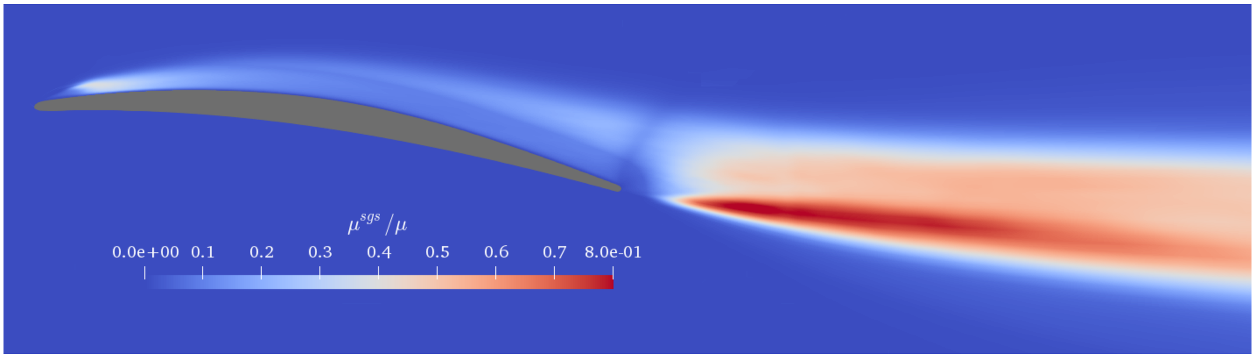

Figure 5.12: Average value of the ratio of the subgrid scale viscosity (from the WALE model) to the true viscosity, for the LES of the case M = 0.4.

observed close to the LE ($x = -0.95$) and close to the TE ($x = -0.02$) at high frequency. Close to the LE ($x = -0.95$), all curves exhibit three main peaks (one at low frequency and two at high frequency), likely due to the separation bubble. While the location of these peaks does not change significantly, their amplitude does depend on the Mach number: the higher the Mach number, the lower the amplitude. One possible explanation comes from the dependence of the size of the separation bubble to the Mach number: as the Mach number increases, the end of the separation bubble is moved downstream, and the location $x = -0.95$ is relatively closer to the beginning of the bubble where the fluctuations are weaker. A different behaviour is observed close to the TE ($x = -0.02$). For M = 0.2 the PSD decreases at a steady rate. However, when the Mach number is increased the high frequency pressure spectrum starts growing: at M = 0.5 one can clearly identify a peak at high frequency. As for the hydrodynamic field and the boundary layer characteristics, it is observed from Fig. 5.13 that the LES and DNS agree closely for the prediction of the surface pressure spectrum. For most of the suction side the surface pressure spectrum predicted by the LES collapses almost exactly with the DNS prediction. As expected, the largest discrepancy is observed close to the LE, where the transition to turbulence takes place.

In wavenumber space, the surface pressure spectrum is described by:

$$\phi_{pp}(k_x, \omega) = \left| \mathcal{F}_t \, \mathcal{F}_x \left[p'(x,t) \right] \right|^2, \tag{5.7}$$

where $\mathcal{F}_t$ (resp. $\mathcal{F}_x$) denotes the Fourier transform with respect to time (resp. streamwise coordinate). Fig. 5.14 displays $\phi_{pp}(k_x, \omega)$ on the aerofoil upper and lower surfaces for the four Mach number cases. This representation of the surface pressure spectrum allows the identification the velocity u_c of the waves along the aerofoil by matching $u_c = \omega/k_x$ with the maxima of the spectra [75]. On the suction side, two convection speeds can be identified: $u_c \approx U_0$ corresponding to the speed of the hydrodynamic fluctuations initially generated at the transition point, and $u_c \approx U_0 + U_0/\mathrm{M}$ corresponding to the downstream propagating acoustic waves. The associated waves extend up to high frequencies. On the pressure side, the negative convection speed $u_c \approx U_0 - U_0/\mathrm{M}$ can be identified, and corresponds to the upstream propagating acoustic waves. Those waves only extend over a low frequency

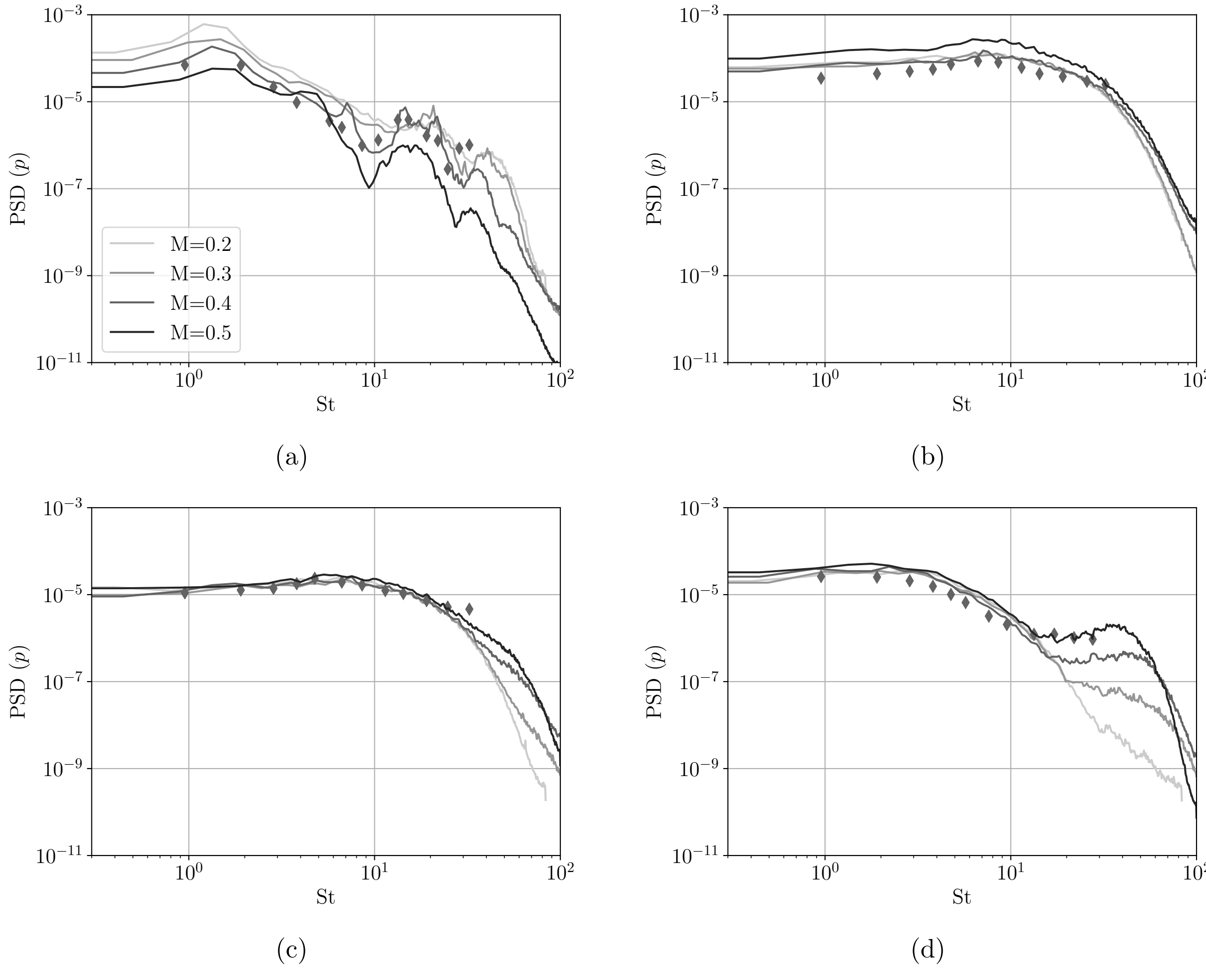

Figure 5.13: Span-averaged surface pressure spectrum for the four Mach numbers. LES results (solid lines) and DNS results for M = 0.4 (diamonds). Four different locations along the suction side: $x = -0.95$ (a), $x = -0.70$ (b), -0.40 (c), -0.02 (d).

range. The Mach number appears to have little influence on the region of the wavenumber spectra associated with the hydrodynamic fluctuations (close to the solid lines in Fig. 5.14), however it has a significant impact on the region of the wavenumber spectra associated with the acoustic waves (close to the dotted lines in Fig. 5.14). When the Mach number is increased, the wavenumber spectrum of the acoustic waves displays a higher amplitude, and extends over a larger frequency range. In the following sections, it is shown that the downstream propagating acoustic waves on the suction side are associated with the high frequency transition/reattachment noise source, while the upstream propagating acoustic waves on the pressure side are associated with the low frequency TE noise source. This latter noise source is also expected to generate upstream waves on the suction side; those waves are most likely not visible in Fig. 5.14 because of the high amplitude of the low frequency hydrodynamic fluctuations.

Finally, peaks are observed at discrete frequencies along the upper surface, in the acoustic part of the wavenumber spectra. Those peaks have a small negative streamwise wavenumber, and are found at a fundamental frequency ω_1 and its harmonics: for $\mathrm{M} = [0.2, 0.3, 0.4, 0.5]$ it is found that $\omega_1 = [102, 66, 45, 31]$. As illustrated in Fig. 5.15 for $\mathrm{M} = 0.4$, those discrete frequencies appear to be related to acoustic modes of discrete spanwise wavenumbers, imposed by the periodicity of the computational domain. The frequency of those modes can be estimated with theoretical considerations. In the approximate theory of geometrical acoustics, the phase velocity vector $\vec{v}_\phi$ of the acoustic waves travelling in the xz plane is:

$$\vec{v}_\phi = u\,\vec{e}_x + c\,(\cos\theta\,\vec{e}_x + \sin\theta\,\vec{e}_z), \tag{5.8}$$

where u is the convective velocity, c is the speed of sound, and θ is the direction of propagation if the coordinate system is moving with the local ambient fluid velocity. With the non-dimensionalisation used in the present study, Eq. (5.8) becomes:

$$\vec{v}_\phi = \left(1 + \frac{1}{\mathrm{M}}\cos\theta\right)\vec{e}_x + \frac{1}{\mathrm{M}}\sin\theta\,\vec{e}_z. \tag{5.9}$$

For the waves travelling along the z direction, the value of θ must be such that $\vec{v}_\phi \cdot \vec{e}_x = 0$, i.e. $\cos\theta = -\mathrm{M}$, and so the magnitude of the phase velocity is:

$$v_\phi = \frac{1}{\mathrm{M}}\sin\theta = \frac{1}{\mathrm{M}}\sqrt{1 - (\cos\theta)^2} = \frac{1}{\mathrm{M}}\sqrt{1 - \mathrm{M}^2} = \frac{\beta}{\mathrm{M}}, \tag{5.10}$$

where $\beta = \sqrt{1 - \mathrm{M}^2}$. Because of the periodicity of the domain in the spanwise direction (the spanwise extent of the computational domain being $L_z = 0.3$ in the present study), the spanwise acoustic modes can only be observed at discrete frequencies ω_n, where n denotes the rank of the harmonics. Those frequencies obey the following equation:

$$\omega_n = 2\pi n \frac{v_\phi}{L_z} = 2\pi n \frac{\beta}{L_z \mathrm{M}}. \tag{5.11}$$

As it can be seen in Fig. 5.16, the fundamental frequency ω_1 measured in the LES matches the prediction of Eq. (5.11) closely for all the Mach numbers, which confirms that the discrete

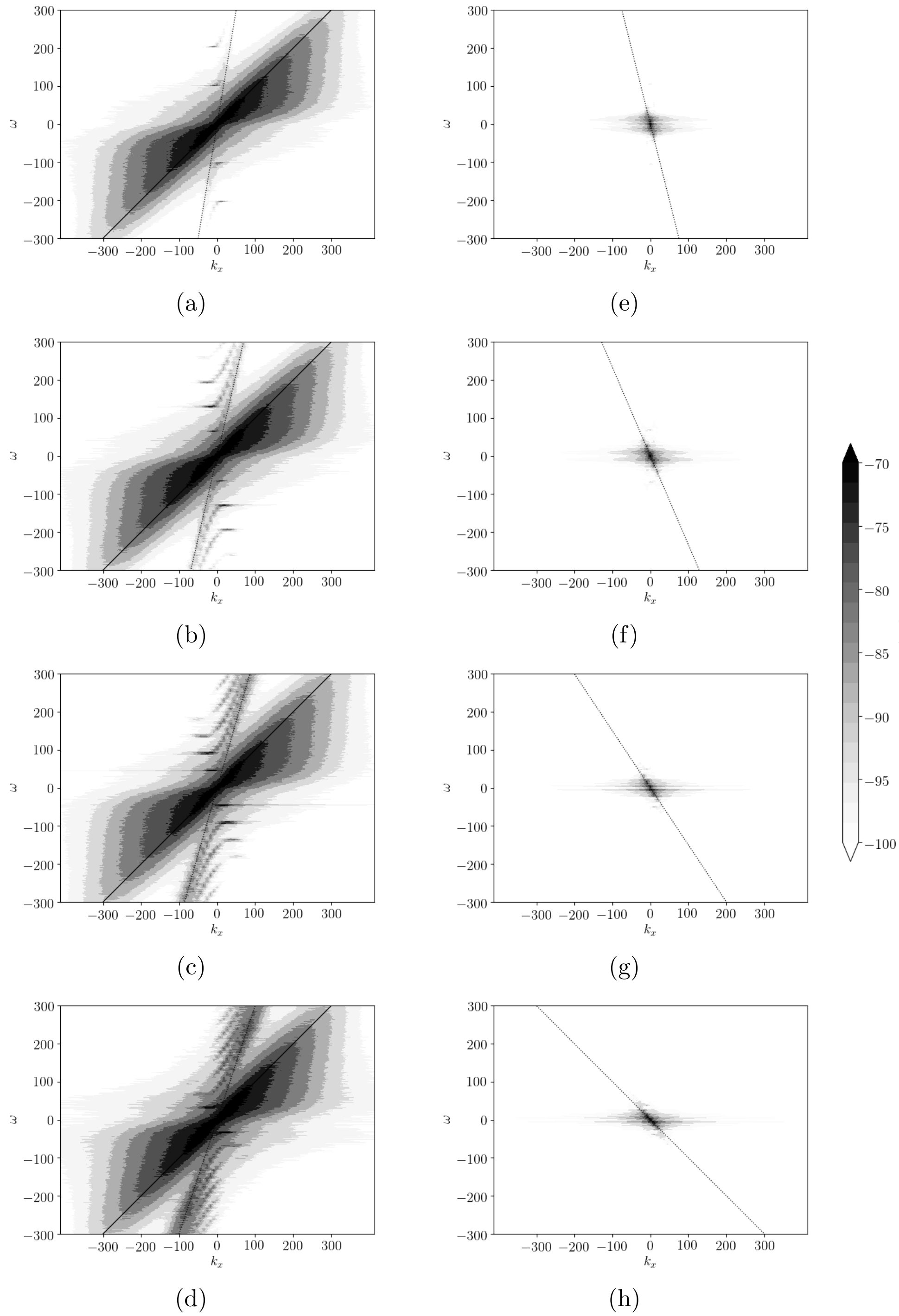

Figure 5.14: Surface pressure spectra in the wavenumber space. The solid lines highlight the convection speed of the hydrodynamic fluctuations U_0, and the dotted lines highlight the speed of the acoustic waves $U_0 \pm U_0/\mathrm{M}$. LES results. Upper surface: $\mathrm{M} = 0.2$ (a), 0.3 (b), 0.4 (c), 0.5 (d); and lower surface: $\mathrm{M} = 0.2$ (e), 0.3 (f), 0.4 (g), 0.5 (h).

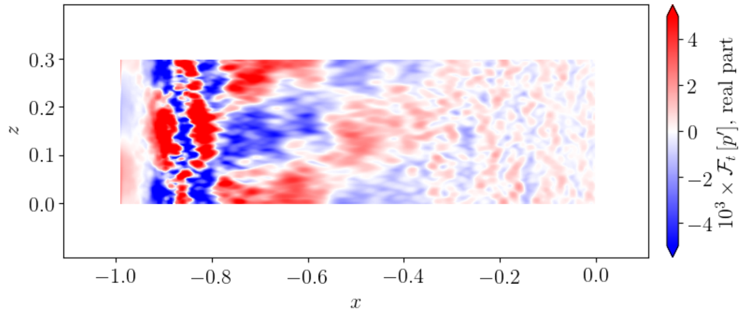

Figure 5.15: Fourier transform of the surface pressure along the upper surface, at $\omega_1 = 45$, $\mathrm{M} = 0.4$. LES results.

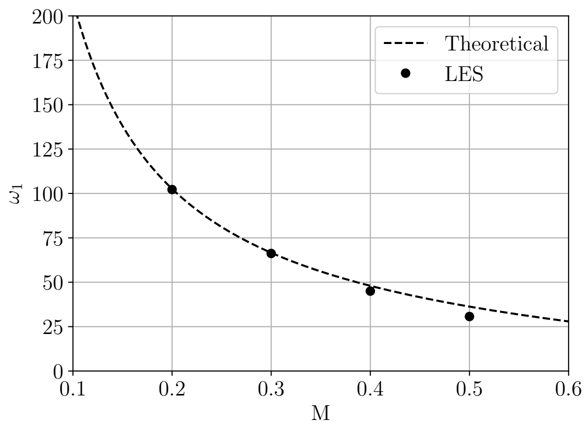

Figure 5.16: Frequency of the fundamental spanwise acoustic mode in function of the Mach number. Comparison between the theoretical frequency (dashed line) and the frequency measured from the LES (dots).

peak frequencies observed in Fig. 5.14 are consequences of the spanwise periodicity of the computational domain.

5.5 Acoustic field

An instantaneous picture of the field of $\nabla \cdot \vec{u}'$ is shown in Fig. 5.17 along with contours of entropy $s = \log(p/\rho^\gamma)$. Fig. 5.17 corresponds to the case $\mathrm{M} = 0.4$, the other cases where found to be qualitatively similar. Two main noise sources can be visually identified: the TE and the transition/reattachment region on the upper surface. Contrary to the study of Wu et al. [23], the near wake does not appear to contribute significantly to the self-noise. However, the current case is fundamentally different in that it does not include installation effects and thus the loading of the aerofoil is different. The transition/reattachment noise source appears to be even stronger than the TE noise for this flow configuration, likely

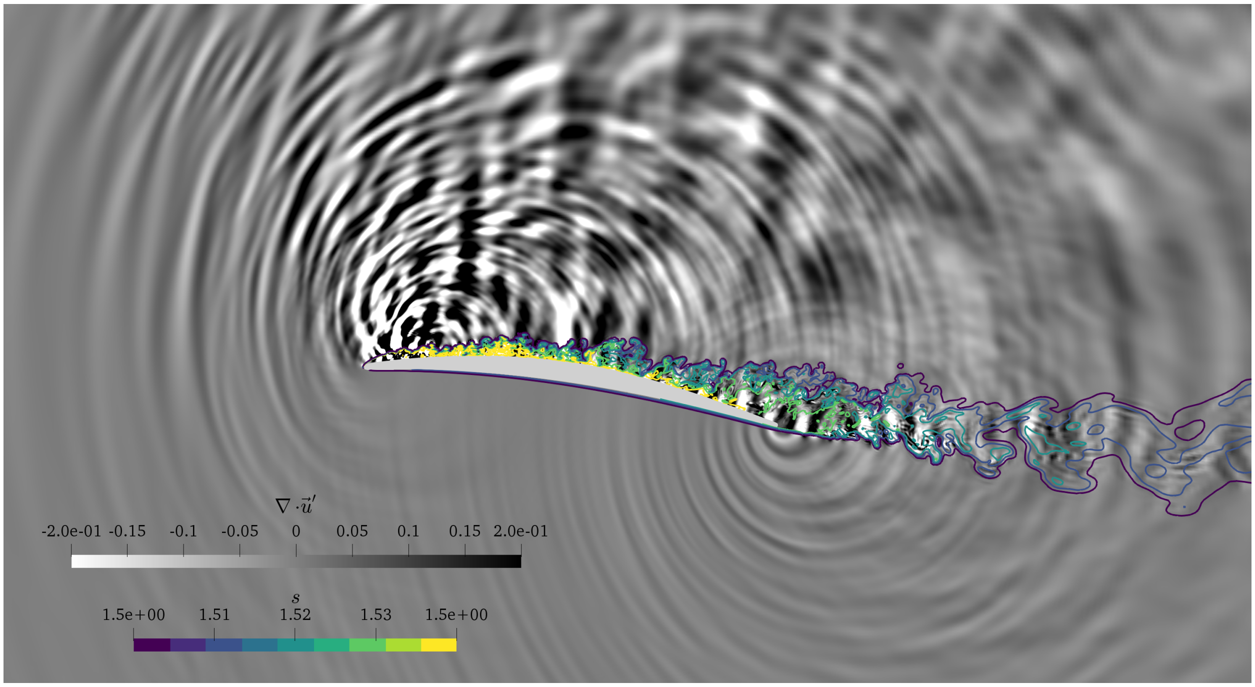

Figure 5.17: Instantaneous field of dilatation rate fluctuations and entropy contours, M = 0.4, DNS results.

because of the high local Mach number due to the strong flow acceleration close to the LE.

Two probes have been placed in the acoustic field at locations symmetric with respect to the horizontal axis: $\vec{x}_{\mathrm{top}} = (-0.5, 1.5, 0)$ and $\vec{x}_{\mathrm{bot}} = (-0.5, -1.5, 0)$. The corresponding pressure signals $p_{\mathrm{top}}(t)$ and $p_{\mathrm{bot}}(t)$ have been saved. The transition/reattachment noise source radiates mostly upwards as it is shielded by the aerofoil surface (with only a slight diffraction at the LE), whereas the TE shows an anti-symmetric pattern on each side of the aerofoil, as expected from classical TE noise theories. Consequently, the bottom probe should contain almost exclusively the TE noise signal $p_{\mathrm{TE}}(t) \approx p_{\mathrm{bot}}(t)$, while the contribution of the TE noise can be removed from the top probe to isolate the noise signal from the transition/reattachment source: $p_{\mathrm{T/R}}(t) \approx p_{\mathrm{top}}(t) + p_{\mathrm{bot}}(t + \Delta t)$, where Δt accounts for the time difference in the propagation of the TE noise up to each probe. This latter is obtained by finding the location of the largest negative peak in the curve of the cross correlation between $p_{\mathrm{top}}(t)$ and $p_{\mathrm{bot}}(t)$. The PSD of p_{TE} and $p_{\mathrm{T/R}}$ for the different cases are presented in Fig. 5.18.

The TE noise displays a low frequency, broadband spectrum, with most of the energy of the signal below St = 2. For the four Mach number cases, little difference is observed in the shape of the curve. For M = 0.3 and M = 0.4, not only the shape of the curve but also the absolute level is very similar, whereas for M = 0.5 the absolute level is larger.

In contrast to the TE noise, the transition/reattachment noise source has a strong tonal contribution. A peak is observed in the PSD, with a frequency which depends on the Mach number. For M = $[0.2, 0.3, 0.4, 0.5]$ the peak frequencies are St $\approx [16.3, 10.5, 7.8, 5.6]$: the

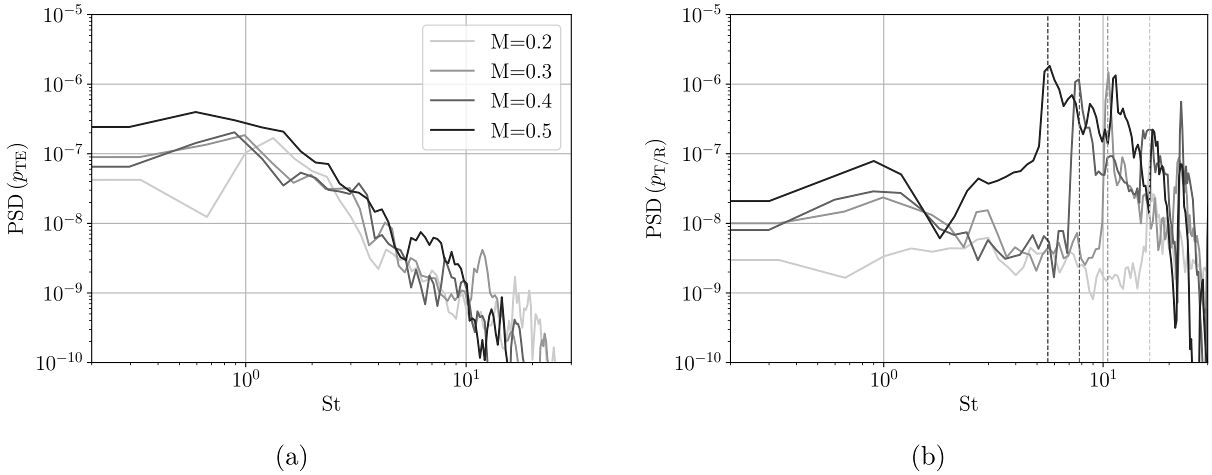

Figure 5.18: PSD of p_{TE} (a) and $p_{\mathrm{T/R}}$ (b). The dashed lines identify the frequency of the first peak in the PSD of $p_{\mathrm{T/R}}$. LES results.

peak frequency decreases as the Mach number increases. At lower frequencies, the broadband part of the spectrum is well below the tone peak. This broadband component is one order of magnitude smaller than the TE noise, proving that the procedure of computing $p_{\mathrm{T/R}}$ form $p_{\mathrm{top}}(t)$ and $p_{\mathrm{bot}}(t)$ successfully removed the contribution of TE noise.

5.6 Pressure cross correlations

Similarly to Jones et al. [76], cross correlations between the aerofoil surface pressure and the far-field pressure were used to further investigate the noise sources. The pressure cross correlation $C_{pp}(\vec{x}_{\mathrm{s}}, \vec{x}_{\mathrm{ff}}, \Delta t)$ between the surface pressure $p_{\mathrm{s}}(\vec{x}_{\mathrm{s}}, t)$ at a point $\vec{x}_{\mathrm{s}}$ along the aerofoil surface and the far-field pressure $p_{\mathrm{ff}}(\vec{x}_{\mathrm{ff}}, t)$ at a point $\vec{x}_{\mathrm{ff}}$ in the acoustic far-field is defined as:

$$C_{pp}(\vec{x}_{\mathrm{s}}, \vec{x}_{\mathrm{ff}}, \Delta t) = \int_{-\infty}^{\infty} p_{\mathrm{s}}(\vec{x}_{\mathrm{s}}, t)\, p_{\mathrm{ff}}(\vec{x}_{\mathrm{ff}}, t + \Delta t)\, \mathrm{d}t. \tag{5.12}$$

For positive values of Δt, p_{ff} is lagging behind p_{s}. Practically, the bounds of the integral in Eq. (5.12) are replaced by a finite time window which is considered periodic, so that the cross correlation can be evaluated as:

$$C_{pp} = \mathcal{F}_t^{-1}\left[\mathcal{F}_t(p_{\mathrm{s}})^* \, \mathcal{F}_t(p_{\mathrm{ff}})\right]. \tag{5.13}$$

If $\vec{x}_{\mathrm{s}}$ corresponds to the location of a noise source which radiates up to $\vec{x}_{\mathrm{ff}}$, then one would expect $C_{pp}(\vec{x}_{\mathrm{s}}, \vec{x}_{\mathrm{ff}}, \Delta t)$ to reach a maximum for $\Delta t = \Delta t_{\mathrm{s}\to\mathrm{ff}}(\vec{x}_{\mathrm{s}}, \vec{x}_{\mathrm{ff}})$, where $\Delta t_{\mathrm{s}\to\mathrm{ff}}(\vec{x}_{\mathrm{s}}, \vec{x}_{\mathrm{ff}})$ corresponds to the acoustic propagation time from $\vec{x}_{\mathrm{s}}$ to $\vec{x}_{\mathrm{ff}}$. Consequently, the location of noise sources along the aerofoil surface can be identified as the $\vec{x}_{\mathrm{s}}$ coordinates which maximise $C_{pp}(\vec{x}_{\mathrm{s}}, \vec{x}_{\mathrm{ff}}, \Delta t_{\mathrm{s}\to\mathrm{ff}}(\vec{x}_{\mathrm{s}}, \vec{x}_{\mathrm{ff}}))$.

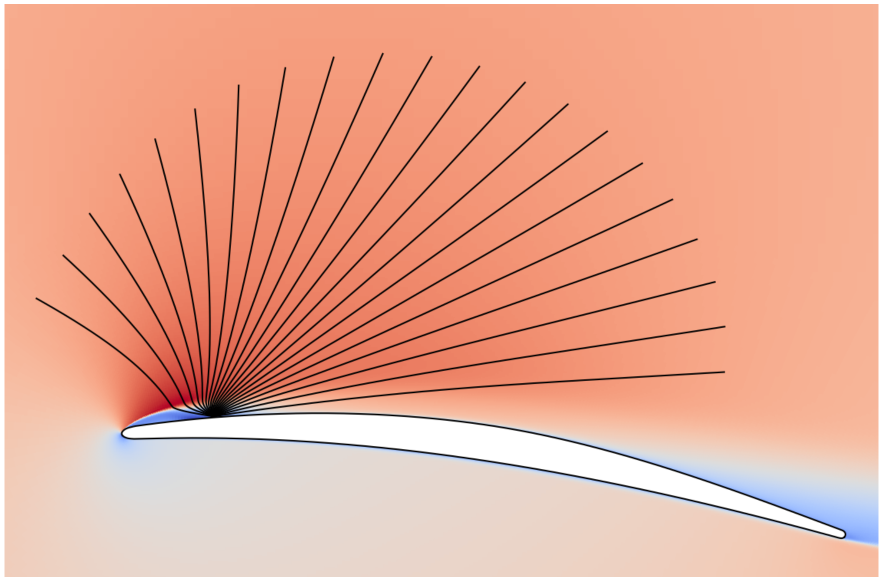

Figure 5.19: Illustration of acoustical ray tracing. The black lines are examples of ray trajectories emitted from a point along the aerofoil surface, and travelling during the same propagation time. The colour map corresponds to the average streamwise velocity field.

Following Jones et al. [76], $\Delta t_{\mathrm{s}\to\mathrm{ff}}(\vec{x}_{\mathrm{s}}, \vec{x}_{\mathrm{ff}})$ is estimated using acoustical ray tracing. In the approximate theory of geometrical acoustics, an acoustic ray is described by a trajectory $\vec{x}(t)$, parametrised by the propagation time t. The acoustic rays obey the following differential equation Pierce [77]:

$$\frac{\mathrm{d}\vec{x}}{\mathrm{d}t} = c(\vec{x}, t)\, \vec{n} \;+\; \vec{u}(\vec{x}, t)\,, \tag{5.14}$$

where $\vec{u}$ is the local ambient fluid velocity, c is the local speed of sound (scalar), and $\vec{n}$ is the unit vector normal to the wavefront ($\vec{n}$ coincides with the direction of propagation if the coordinate system is moving with the local ambient fluid velocity). With the non-dimensionalisation used in the present study, the local speed of sound is $c = \sqrt{T}/\mathrm{M}$. In order to estimate $\Delta t_{\mathrm{s}\to\mathrm{ff}}(\vec{x}_{\mathrm{s}}, \vec{x}_{\mathrm{ff}})$, Eq. (5.14) is integrated numerically with the initial condition $\vec{x}(t = 0) = \vec{x}_{\mathrm{s}}$. The orientation vector $\vec{n}$ is selected such that the ray trajectory includes the point $\vec{x}_{\mathrm{ff}}$ (to do so, different values of $\vec{n}$ are tested iteratively until the correct value is found). The acoustic propagation time from the aerofoil surface to the far-field point is then the value $\Delta t_{\mathrm{s}\to\mathrm{ff}}(\vec{x}_{\mathrm{s}}, \vec{x}_{\mathrm{ff}})$ which is such that $\vec{x}(t = \Delta t_{\mathrm{s}\to\mathrm{ff}}(\vec{x}_{\mathrm{s}}, \vec{x}_{\mathrm{ff}})) = \vec{x}_{\mathrm{ff}}$. An illustration of acoustical ray tracing is presented in Fig. 5.19.

In the following, the two probes used in the previous section are taken as the far-field point: either $\vec{x}_{\mathrm{ff}} = \vec{x}_{\mathrm{top}}$ and $p_{\mathrm{ff}} = p_{\mathrm{top}}$, or $\vec{x}_{\mathrm{ff}} = \vec{x}_{\mathrm{bot}}$ and $p_{\mathrm{ff}} = p_{\mathrm{bot}}$. The pressure cross correlations are presented in Fig. 5.21. This approach appears to work particularly well for TE noise: for every case, high correlation is observed in the TE region when Δt is close to $\Delta t_{\mathrm{s}\to\mathrm{ff}}$ (estimated with acoustical ray tracing). For the low frequencies, which were identified to be related to TE noise, it is observed that $C_{pp}(\vec{x}_{\mathrm{s}}, \vec{x}_{\mathrm{top}}, \Delta t) \approx -C_{pp}(\vec{x}_{\mathrm{s}}, \vec{x}_{\mathrm{bot}}, \Delta t)$, in

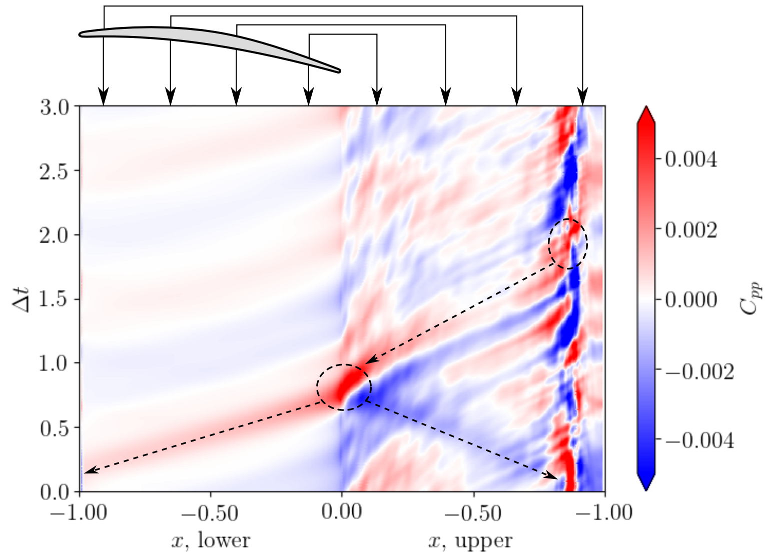

Figure 5.20: Close-up on the pressure cross correlation for p_{bot} and M = 0.4, LES results.

accordance with the anti-symmetric pattern of TE noise. One can see in Fig. 5.20 (reading the figure from top to bottom) that the pressure fluctuations are initially generated in the transition/reattachment region and then are convected along the upper surface, while maintaining a high value of the cross correlation. When the pressure fluctuations reach the TE, the TE noise is emitted and propagates upstream along the aerofoil surface, with opposite sign between the upper and lower surface. Recently, Sano et al. [78] also reported extended regions of high flow-acoustic correlation close to the surface of a NACA0012 aerofoil at zero angle of attack. They concluded that turbulent structures advect over a significant region of the boundary layer maintaining their coherence, prior to TE scattering. This is consistent with the frozen turbulence hypothesis often invoked in simplified analytical models, such as Amiet's model [79]. Those last observations are believed to have significant repercussions on the prediction and modelling of the TE noise when a separation bubble is present. The fact that a high value of the cross correlation is maintained from the end of the separation bubble up to the TE indicates that the TE noise is a direct consequence of the pressure fluctuations generated in the transition/reattachment region at the end of the separation bubble. Consequently, an accurate prediction of the dynamics of the separation bubble seems to be essential to the prediction of the TE noise.

5.7 Summary

The turbulent flow and the noise produced by an isolated CD aerofoil in a uniform flow have been investigated. The Reynolds number is $\mathrm{Re} = 10^5$ and the angle of attack is $\alpha = 8°$. LES have been conducted at four different values of the free-stream Mach number $\mathrm{M} = [0.2, 0.3, 0.4, 0.5]$, and a DNS has been conducted for the case $\mathrm{M} = 0.4$. The good agreement between the LES and DNS for $\mathrm{M} = 0.4$ demonstrated that the LES are suited to

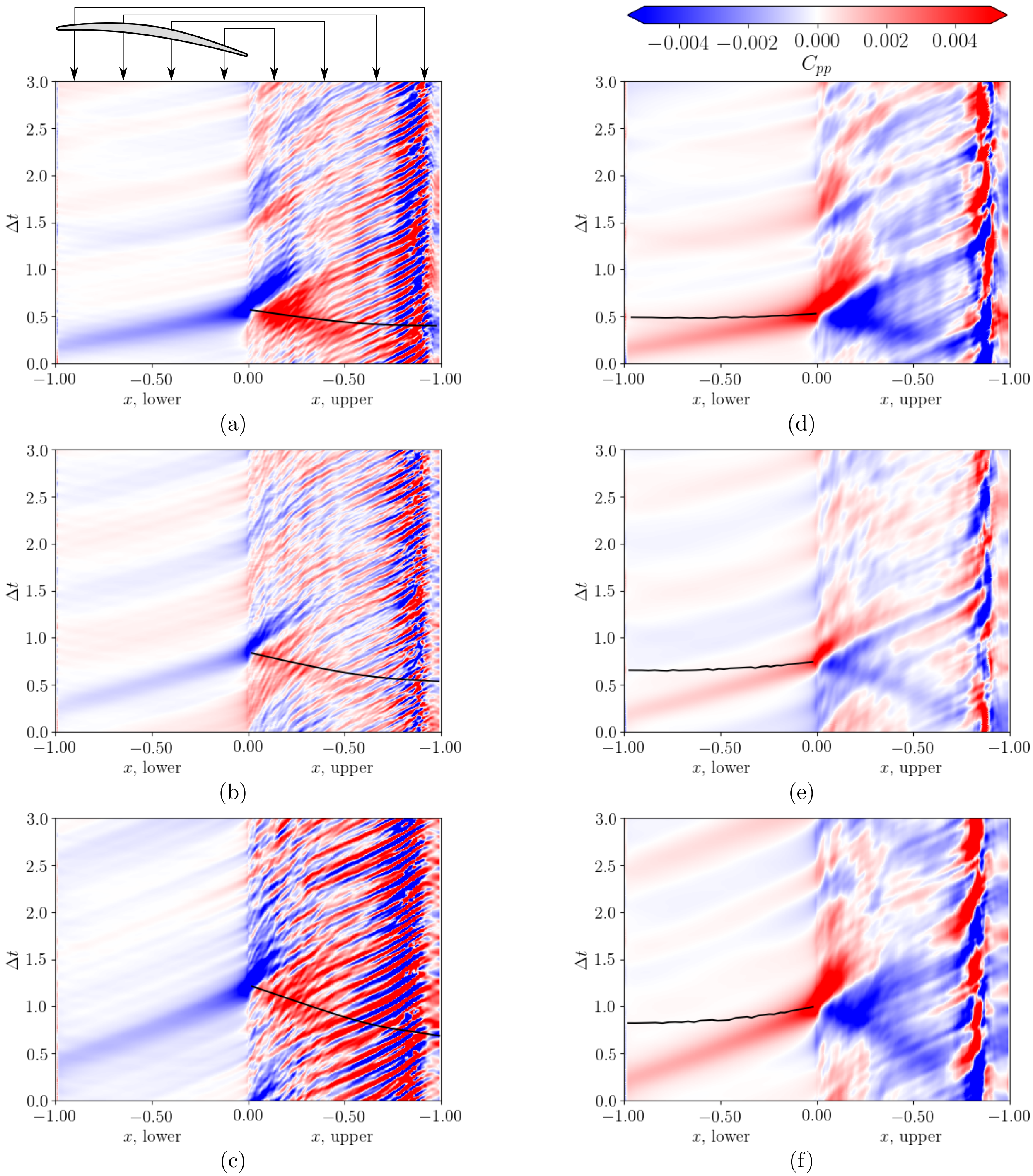

Figure 5.21: Span-averaged cross correlation between the aerofoil surface pressure and the far-field pressure. The solid black lines correspond to the acoustic propagation time from the aerofoil surface to the far-field point, estimated using acoustical ray tracing. LES results. Correlation with p_{top} for M = 0.3 (a), 0.4 (b), 0.5 (c); and with p_{bot} for M = 0.3 (d), 0.4 (e), 0.5 (f).

the accurate numerical simulation of the aerofoil flow.

For all cases, it is observed that the flow along the aerofoil pressure side remains fully laminar up to the TE. Along the suction side, the flow undergoes laminar separation right from the LE, and a separation bubble is formed. Downstream of the LE, transition to turbulence is observed, then the flow reattaches.

The investigation of the pressure and friction coefficients showed that the LE separation bubble is affected by the compressibility: the size of the separation bubble increases as the Mach number increases. The same conclusion was drawn from the analysis of the boundary layer coefficients on the suction side (the definition of those coefficients has been adapted to take into account the spatially varying potential flow in a consistent way).

Surface pressure spectra were computed along the aerofoil upper surface. Along most of the chord, the curves of the PSD display the classical shape for TE noise, i.e. a plateau at low to moderate Strouhal number followed by a sudden drop at higher Strouhal number; and the Mach number seems to have little influence on the surface pressure spectra. However, a different behaviour is observed next to the TE, with a secondary increase of the PSD at high Strouhal number. This high Strouhal number phenomenon taking place next to the TE appears to be highly dependent on the Mach number.

Two main noise sources were identified by analysing the acoustic field: the classical TE noise source, and an additional noise source located in the transition/reattachment region at the end of the LE separation bubble. While the TE noise displays a low frequency broadband spectrum, the transition/reattachment noise source has a strong tonal contribution, with a peak frequency that depends that depends on the Mach number: the higher the Mach number, the lower the peak frequency. Finally, the analysis of the surface/far-field pressure correlation highlighted the anti-symmetric pattern of the TE noise, and showed that the TE noise is direct consequence of the pressure fluctuations generated at the end of the separation bubble.

Chapter 6

Conclusions

6.1 Summary

The flow over a CD aerofoil and the resulting noise have been investigated numerically. The objective was to study the different sources of aerofoil self-noise. While the TE noise source is quite well known and has been investigated extensively during the last decades, the study of other aerofoil self-noise sources is still in its infancy. In this context, the present project aimed to investigate not only the TE noise, but also another noise source that is observed in the flow around the CD aerofoil at the end of the LE separation bubble. Another aspect that has not been covered extensively by previous investigations is the effect of the compressibility on the self-noise sources. As a first step to fill this gap, several different free-stream Mach numbers have been compared in the present study. The methodology of this project consists of conducting DNC in order to investigate both the hydrodynamic and the acoustic fields in detail, and study the physical mechanisms that generate the aerofoil self-noise.

The numerical simulations have been conducted using the in-house CFD solver HiPSTAR. As a part of the present project, an overset grid framework has been implemented in HiPSTAR. This framework has been design to enhance the capabilities of HiPSTAR to handle complex geometries, while maintaining the accuracy of the solver and allowing to employ high-quality grids. In the overset grid method, an interpolation scheme is used to connect separate grids, which eliminates the requirement of point-to-point matching at the interface. The original algorithm used for the generation of the composite grid has been described in detail. An instability due to the uncoupling of multiple different solutions in the overlapping regions of the domain has been described, and a solution to this issue has been presented. Finally, the newly implemented overset grid framework has been validated with two test cases: the convection of an isentropic vortex and the Taylor-Green vortex.

The HiPSTAR solver, in combination with the overset grid method, has been used to conduct four LES and one DNS of the flow around an isolated CD aerofoil. The angle of attack is $\alpha = 8°$, the Reynolds number is $\mathrm{Re} = 10^5$, and four different values of the free-stream Mach number are compared: $\mathrm{M} = [0.2, 0.3, 0.4, 0.5]$.

6.2 Principal findings

For all the four Mach numbers, the flow field looks qualitatively similar. The flow along the pressure side is attached and laminar from the LE to the TE. Along the suction side, the flow separates at the LE, and a laminar separation bubble is formed. A little farther downstream, transition to turbulence is observed, then the flow reattaches and remains turbulent and attached down to the TE. It has been shown that the LE separation bubble is affected by the flow compressibility: the larger the Mach number, the larger the separation bubble. While the Mach number influences the average size of the separation bubble, it is noted that the variance of the size of the separation bubble does not vary significantly.

It has been found that the Mach number has little influence on the surface pressure spectrum along most of the aerofoil suction side, except in the vicinity of the LE and next to the TE. Close to the LE, the surface pressure spectrum exhibits three main peaks, one at low frequency and two at high frequencies. The amplitude of those peaks appears to decrease when the Mach number increases. Next to the TE, an increase is observed in the surface pressure spectrum at high frequency. This phenomenon appears to be highly dependent on the compressibility effects: the larger the Mach number, the larger the increase. To the author's knowledge, it is the first time that this phenomenon is observed.

For each case, the same two noise sources can be identified: the classical TE noise source and an additional noise source in the transition/reattachment region at the end of the separation bubble. The latter radiates mostly upwards as it is shielded by the aerofoil surface. While the TE noise source has a low frequency broadband spectrum, the transition/reattachment noise source presents a strong tone (and some harmonics) at high-frequency. The compressibility has little influence on the noise from the TE noise source, apart from a slight increase of the absolute noise level at high Mach number. On the other hand, the pressure spectrum of the transition/reattachment noise source is strongly influenced by the compressibility: when the Mach number increases, the frequency of the main tone decreases, and the background noise level increases. Finally, the analysis of the pressure cross-correlation between the aerofoil surface and the free-field highlighted an anti-symmetric pattern of the TE noise, and indicated that the TE noise is a direct consequence of the pressure fluctuations generated by the separation bubble.

6.3 Recommendations for future research directions

In the present study, the flow around an isolated CD aerofoil and the resulting self-noise have been investigated extensively. Findings of previous studies have been confirmed, and some new phenomena have been highlighted. However, there still remain avenues of future research.

- This study revealed the presence of a high-frequency increase in the surface pressure spectrum near the TE when the Mach number becomes large enough. To the author's knowledge, it is the first time that such phenomenon is observed. However, no satisfying explanation of this phenomenon has been found so far. As the pressure fluctuations near the TE are very likely to affect the radiated TE noise, further study of this phenomenon is very likely to be relevant in the context of aerofoil noise.

- The present project takes place in the context of turbomachinery. In particular, it is motivated by the increasing demand to reduce the noise from the fans of industrial and domestic ventilation systems, which is mainly produced by the compressor and stator blades. In the present investigation, the geometry of an aerofoil that is actually used in such machines has been selected in order to be representative of practical applications, yet an infinite (periodic) span length has been used. Further DNC studies of an aerofoil with a finite span and/or an end-wall would surely reveal different phenomena, relevant to the context in which stator/compressor blades operate in practical applications. It is noted however that such investigations would likely increase dramatically the computational cost of the numerical simulations, as a much larger domain would be required to account for the non-uniformity in the spanwise direction.

- As mentioned in the previous point, the study of aerofoil self-noise would surely benefit from DNC studies that are as representative as possible of practical applications. In particular, highly-swept blades are often used as a mean to reduce the TE noise in different applications. The importance of taking into account the sweep in a theory of TE noise has recently been highlighted [80]. Contrary to the previous point, the effect of the sweep could be included in a DNC study without significant increase of the computational cost compared to the no-sweep case. The addition of a cross-flow could be an interesting first step towards the DNC study of a compressor blade in a realistic environment.

Bibliography

[1] WHO regional office for Europe, *Burden of disease from environmental noise: Quantification of healthy life years lost in Europe*, World Health Organization, 2011.

[2] Brueckner, J. K., and Girvin, R., "Airport noise regulation, airline service quality, and social welfare," *Transportation Research Part B: Methodological*, Vol. 42, No. 1, 2008, pp. 19–37. doi:10.1016/j.trb.2007.05.005.

[3] Roger, M., and Moreau, S., "Broadband self noise from loaded fan blades," *AIAA Journal*, Vol. 42, No. 3, 2004, pp. 536–544. doi:10.2514/1.9108.

[4] Brooks, T. F., Pope, D. S., and Marcolini, M. A., "Airfoil self-noise and prediction," Tech. rep., NASA Langley Research Center, 1989.

[5] Leylekian, L., Lebrun, M., and Lempereur, P., "An overview of aircraft noise reduction technologies," *AerospaceLab*, Vol. 7, 2014, pp. 1–15. doi:10.12762/2014.AL07-01.

[6] Radespiel, R., and Heinze, W., "SFB 880: fundamentals of high lift for future commercial aircraft," *CEAS Aeronautical Journal*, Vol. 5, No. 3, 2014, pp. 239–251. doi:10.1007/s13272-014-0103-6.

[7] Oerlemans, S., Sijtsma, P., and Méndez López, B., "Location and quantification of noise sources on a wind turbine," *Journal of Sound and Vibration*, Vol. 299, No. 4-5, 2007, pp. 869–883. doi:10.1016/j.jsv.2006.07.032.

[8] Bianchi, S., Corsini, A., and Sheard, A. G., "A critical review of passive noise control techniques in industrial fans," *Journal of Engineering for Gas Turbines and Power*, Vol. 136, No. 4, 2014, p. 044001. doi:10.1115/1.4025837.

[9] Amiet, R. K., "Acoustic radiation from an airfoil in a turbulent stream," *Journal of Sound and Vibration*, Vol. 41, No. 4, 1975, pp. 407–420. doi:10.1016/s0022-460x(75)80105-2.

[10] Sandberg, R. D., and Jones, L. E., "Direct numerical simulations of airfoil self-noise," *Procedia Engineering*, Vol. 6, 2010, pp. 274–282. doi:10.1016/j.proeng.2010.09.029.

[11] Sandberg, R. D., "Compressible-flow DNS with application to airfoil noise," *Flow, Turbulence and Combustion*, Vol. 95, No. 2, 2015, pp. 211–229. doi:10.1007/s10494-015-9617-1.

[12] Desquesnes, G., Terracol, M., and Sagaut, P., "Numerical investigation of the tone noise mechanism over laminar airfoils," *Journal of Fluid Mechanics*, Vol. 591, 2007, pp. 155–182. doi:10.1017/S0022112007007896.

[13] Sandberg, R. D., Jones, L. E., Sandham, N. D., and Joseph, P. F., "Direct numerical simulations of noise generated by airfoil trailing edges," *13th AIAA/CEAS Aeroacoustics Conference*, American Institute of Aeronautics and Astronautics, Rome, Italy, 2007, p. 3469. doi:10.2514/6.2007-3469.

[14] Sandberg, R. D., Jones, L. E., and Sandham, N. D., "Direct numerical simulations of noise generated by turbulent flow over airfoils," *14th AIAA/CEAS Aeroacoustics Conference*, American Institute of Aeronautics and Astronautics, Vancouver, Canada, 2008, p. 2861. doi:10.2514/6.2008-2861.

[15] Marsden, O., Bogey, C., and Bailly, C., "Direct noise computation of the turbulent flow around a zero-incidence airfoil," *AIAA Journal*, Vol. 46, No. 4, 2008, pp. 874–883. doi:10.2514/1.29825.

[16] Jones, L. E., and Sandberg, R. D., "Numerical investigation of tonal airfoil self-noise generated by an acoustic feedback-loop," *16th AIAA/CEAS Aeroacoustics Conference*, American Institute of Aeronautics and Astronautics, Stockholm, Sweden, 2010, p. 3701. doi:10.2514/6.2010-3701.

[17] Jones, L. E., and Sandberg, R. D., "Numerical analysis of tonal airfoil self-noise and acoustic feedback-loops," *Journal of Sound and Vibration*, Vol. 330, No. 25, 2011, pp. 6137–6152. doi:10.1016/j.jsv.2011.07.009.

[18] Sanjosé, M., Moreau, S., Kim, M.-S., and Pérot, F., "Direct self-noise simulation of the installed Controlled Diffusion airfoil," *17th AIAA/CEAS Aeroacoustics Conference*, American Institute of Aeronautics and Astronautics, Portland, Oregon, 2011, p. 2716. doi:10.2514/6.2011-2716.

[19] Tam, C. K. W., and Ju, H., "Aerofoil tones at moderate Reynolds number," *Journal of Fluid Mechanics*, Vol. 690, 2012, pp. 536–570. doi:10.1017/jfm.2011.465.

[20] Winkler, J., Sandberg, R. D., and Moreau, S., "Direct numerical simulation of the self-noise radiated by an airfoil in a narrow stream," *18th AIAA/CEAS Aeroacoustics Conference*, American Institute of Aeronautics and Astronautics, Colorado Springs, Colorado, 2012, p. 2059. doi:10.2514/6.2012-2059.

[21] Ramírez, W. A., and Wolf, W. R., "Effects of trailing edge bluntness on airfoil tonal noise at low Reynolds numbers," *Journal of the Brazilian Society of Mechanical Sciences and Engineering*, Vol. 38, No. 8, 2016, pp. 2369–2380. doi:10.1007/s40430-015-0308-6.

[22] Ffowcs Williams, J. E., and Hawkings, D. L., "Sound generation by turbulence and surfaces in arbitrary motion," *Philosophical Transactions of the Royal Society of London A*, Vol. 264, No. 1151, 1969, pp. 321–342. doi:10.1098/rsta.1969.0031.

[23] Wu, H., Sanjosé, M., Moreau, S., and Sandberg, R. D., "Direct Numerical Simulation of the Self-Noise Radiated by the Installed Controlled-Diffusion Airfoil at Transitional Reynolds Number," *24th AIAA/CEAS Aeroacoustics Conference*, American Institute of Aeronautics and Astronautics, Atlanta, Georgia, 2018, p. 3797. doi:10.2514/6.2018-3797.

[24] Moreau, S., and Roger, M., "Effect of airfoil aerodynamic loading on trailing edge noise sources," *AIAA Journal*, Vol. 43, No. 1, 2005, pp. 41–52. doi:10.2514/1.5578.

[25] Christophe, J., and Moreau, S., "LES of the trailing-edge flow and noise of a controlled-diffusion airfoil at high angle of attack," *Center for Turbulence Research, Annual Research Briefs, Stanford University*, 2008, pp. 305–316.

[26] Christophe, J., Moreau, S., Hamman, C. W., Witteveen, J. A. S., and Iaccarino, G., "Uncertainty quantification for the trailing-edge noise of a controlled-diffusion airfoil," *AIAA Journal*, Vol. 53, No. 1, 2015, pp. 42–54. doi:10.2514/1.J051696.

[27] Martínez-Lera, P., Christophe, J., and Schram, C., "Computation of the self-noise of a controlled-diffusion airfoil based on the acoustic analogy," *International Journal of Aeroacoustics*, Vol. 16, No. 1-2, 2017, pp. 44–64. doi:10.1177/1475472X16680447.

[28] White, F. M., *Viscous fluid flow*, McGraw-Hill, 1991.

[29] Sutherland, W., "The viscosity of gases and molecular force," *The London, Edinburgh, and Dublin Philosophical Magazine and Journal of Science*, Vol. 36, No. 223, 1893, pp. 507–531. doi:10.1080/14786449308620508.

[30] Leonard, A., "Energy cascade in large-eddy simulations of turbulent fluid flows," *Advances in geophysics*, Vol. 18, Elsevier, 1975, pp. 237–248. doi:10.1016/S0065-2687(08)60464-1.

[31] Adumitroaie, V., Ristorcelli, J. R., and Taulbee, D. B., "Progress in Favre-Reynolds stress closures for compressible flows," *Physics of Fluids*, Vol. 11, No. 9, 1998, pp. 2696–2719. doi:10.1063/1.870130.

[32] Nicoud, F., and Ducros, F., "Subgrid-scale stress modelling based on the square of the velocity gradient tensor," *Flow, Turbulence and Combustion*, Vol. 62, No. 3, 1999, pp. 183–200. doi:10.1023/a:1009995426001.

[33] Michelassi, V., Chen, L.-W., Pichler, R., and Sandberg, R. D., "Compressible direct numerical simulation of low-pressure turbines–Part II: effect of inflow disturbances," *Journal of Turbomachinery*, Vol. 137, No. 7, 2015, p. 071005. doi:10.1115/1.4029126.

[34] Scillitoe, A. D., Tucker, P. G., and Adami, P., "Numerical investigation of three-dimensional separation in an axial flow compressor: the influence of freestream turbulence intensity and endwall boundary layer state," *Journal of Turbomachinery*, Vol. 139, No. 2, 2017, p. 021011. doi:10.1115/1.4034797.

[35] Carpenter, M. H., Nordström, J., and Gottlieb, D., "A stable and conservative interface treatment of arbitrary spatial accuracy," *Journal of Computational Physics*, Vol. 148, No. 2, 1999, pp. 341–365. doi:10.1006/jcph.1998.6114.

[36] Kennedy, C. A., Carpenter, M. H., and Lewis, R. M., "Low-storage, explicit Runge–Kutta schemes for the compressible Navier–Stokes equations," *Applied Numerical Mathematics*, Vol. 35, No. 3, 2000, pp. 177–219. doi:10.1016/S0168-9274(99)00141-5.

[37] Bogey, C., and Bailly, C., "A family of low dispersive and low dissipative explicit schemes for flow and noise computations," *Journal of Computational Physics*, Vol. 194, No. 1, 2004, pp. 194–214. doi:10.1016/j.jcp.2003.09.003.

[38] Kennedy, C. A., and Gruber, A., "Reduced aliasing formulations of the convective terms within the Navier–Stokes equations for a compressible fluid," *Journal of Computational Physics*, Vol. 227, No. 3, 2008, pp. 1676–1700. doi:10.1016/j.jcp.2007.09.020.

[39] Jones, L. E., "Numerical studies of the flow around an airfoil at low Reynolds number," Ph.D. thesis, University of Southampton, 2008.

[40] Kim, J. W., and Lee, D. J., "Characteristic interface conditions for multiblock high-order computation on singular structured grid," *AIAA Journal*, Vol. 41, No. 12, 2003, pp. 2341–2348. doi:10.2514/2.6858.

[41] Tam, C. K. W., and Hu, F. Q., "An optimized multi-dimensional interpolation scheme for computational aeroacoustics applications using overset grid," *10th AIAA/CEAS Aeroacoustics Conference*, American Institute of Aeronautics and Astronautics, Manchester, Great Britain, 2004, p. 2812. doi:10.2514/6.2004-2812.

[42] Magnus, R., and Yoshihara, H., "Inviscid transonic flow over airfoils," *AIAA Journal*, Vol. 8, No. 12, 1970, pp. 2157–2162. doi:10.2514/3.6080.

[43] Atta, E. H., "Component-adaptive grid interfacing," *19th Aerospace Sciences Meeting*, American Institute of Aeronautics and Astronautics, 1981, p. 382. doi:10.2514/6.1981-382.

[44] Benek, J. A., Steger, J. L., and Dougherty, F. C., "A flexible grid embedding technique with application to the Euler equations," *6th Computational Fluid Dynamics Conference Danvers*, 1983, p. 1944. doi:10.2514/6.1983-1944.

[45] Benek, J. A., Buning, P. G., and Steger, J. L., "A 3-D chimera grid embedding technique," *7th Computational Physics Conference*, American Institute of Aeronautics and Astronautics, 1985, p. 1523. doi:10.2514/6.1985-1523.

[46] Sherer, S. E., and Scott, J. N., "High-order compact finite-difference methods on general overset grids," *Journal of Computational Physics*, Vol. 210, No. 2, 2005, pp. 459–496. doi:10.1016/j.jcp.2005.04.017.

[47] Desquesnes, G., Terracol, M., Manoha, E., and Sagaut, P., "On the use of a high order overlapping grid method for coupling in CFD/CAA," *Journal of Computational Physics*, Vol. 220, No. 1, 2006, pp. 355–382. doi:10.1016/j.jcp.2006.05.019.

[48] Wolf, W. R., Azevedo, J. L. F., and Lele, S. K., "Convective effects and the role of quadrupole sources for aerofoil aeroacoustics," *Journal of Fluid Mechanics*, Vol. 708, 2012, pp. 502–538. doi:10.1017/jfm.2012.327.

[49] Sherer, S. E., "Investigation of high-order and optimized interpolation methods with implementation in a high-order overset grid fluid dynamics solver," Ph.D. thesis, The Ohio State University, 2002.

[50] Deuse, M., and Sandberg, R. D., "Parametric study of multiple aerofoil self-noise sources using direct noise computation," *25th AIAA/CEAS Aeroacoustics Conference*, American Institute of Aeronautics and Astronautics, Delft, The Netherlands, 2019, p. 2681. doi:10.2514/6.2019-2681.

[51] Wagner, G. A., Deuse, M., Illingworth, S. J., and Sandberg, R. D., "Resolvent analysis-based pressure modeling for trailing edge noise prediction," *25th AIAA/CEAS Aeroacoustics Conference*, American Institute of Aeronautics and Astronautics, Delft, The Netherlands, 2019, p. 2720. doi:10.2514/6.2019-2720.

[52] Jiang, W., Zhang, Y., and Yang, A., "Numerical simulations of complex aircraft configurations using structured overset grids with implicit hole-cutting," *Aerospace Science and Technology*, Vol. 94, 2019, p. 105402. doi:10.1016/j.ast.2019.105402.

[53] Belk, D., and Maple, R., "Automated assembly of structured grids for moving body problems," *12th Computational Fluid Dynamics Conference*, 1995, p. 1680. doi:10.2514/6.1995-1680.

[54] Wang, Z., and Parthasarathy, V., "A fully automated Chimera methodology for multiple moving body problems," *International Journal for Numerical Methods in Fluids*, Vol. 33, No. 7, 2000, pp. 919–938. doi:10.1002/1097-0363(20000815)33:7<919::AID-FLD944>3.0.CO;2-G.

[55] Meakin, R., "Object X-rays for cutting holes in composite overset structured grids," *15th AIAA computational fluid dynamics conference*, American Institute of Aeronautics and Astronautics, 2001, p. 2537. doi:10.2514/6.2001-2537.

[56] Henshaw, W., "Overture: An object-oriented framework for overlapping grid applications," *32nd AIAA Fluid Dynamics Conference and Exhibit*, American Institute of Aeronautics and Astronautics, 2002, p. 3189. doi:10.2514/6.2002-3189.

[57] Suhs, N., Rogers, S., and Dietz, W., "PEGASUS 5: An automated pre-processor for overset-grid CFD," *32nd AIAA Fluid Dynamics Conference and Exhibit*, American Institute of Aeronautics and Astronautics, 2002, p. 3186. doi:10.2514/6.2002-3186.

[58] Chesshire, G., and Henshaw, W. D., "Composite overlapping meshes for the solution of partial differential equations," *Journal of Computational Physics*, Vol. 90, No. 1, 1990, pp. 1–64. doi:10.1016/0021-9991(90)90196-8.

[59] Bodony, D. J., Zagaris, G., Reichert, A., and Zhang, Q., "Provably stable overset grid methods for computational aeroacoustics," *Journal of Sound and Vibration*, Vol. 330, No. 17, 2011, pp. 4161–4179. doi:10.1016/j.jsv.2011.02.010.

[60] Reichert, A., Heath, M. T., and Bodony, D. J., "Energy stable numerical methods for hyperbolic partial differential equations using overlapping domain decomposition," *Journal of Computational Physics*, Vol. 231, No. 16, 2012, pp. 5243–5265. doi:10.1016/j.jcp.2012.03.003.

[61] Sharan, N., Pantano, C., and Bodony, D. J., "Time-stable overset grid method for hyperbolic problems using summation-by-parts operators," *Journal of Computational Physics*, Vol. 361, 2018, pp. 199–230. doi:10.1016/j.jcp.2018.01.049.

[62] Pulliam, T., "High order accurate finite-difference methods: as seen in OVERFLOW," *20th AIAA Computational Fluid Dynamics Conference*, American Institute of Aeronautics and Astronautics, 2011, p. 3851. doi:10.2514/6.2011-3851.

[63] Carpenter, M. H., Gottlieb, D., and Abarbanel, S., "Time-stable boundary conditions for finite-difference schemes solving hyperbolic systems: methodology and application to high-order compact schemes," *Journal of Computational Physics*, Vol. 111, No. 2, 1994, pp. 220–236. doi:10.1006/jcph.1994.1057.

[64] Yee, H. C., Sandham, N. D., and Djomehri, M. J., "Low-dissipative high-order shock-capturing methods using characteristic-based filters," *Journal of Computational Physics*, Vol. 150, No. 1, 1999, pp. 199–238. doi:10.1006/jcph.1998.6177.

[65] Taylor, G. I., and Green, A. E., "Mechanism of the production of small eddies from large ones," *Proceedings of the Royal Society of London. Series A, Mathematical and Physical Sciences*, Vol. 158, No. 895, 1937, pp. 499–521. doi:10.1098/rspa.1937.0036.

[66] DeBonis, J. R., "Solutions of the Taylor-Green vortex problem using high-resolution explicit finite difference methods," *51st AIAA Aerospace Sciences Meeting including the New Horizons Forum and Aerospace Exposition*, American Institute of Aeronautics and Astronautics, 2013, p. 382. doi:10.2514/6.2013-382.

[67] Jammy, S. P., Jacobs, C. T., and Sandham, N. D., "Enstrophy and kinetic energy data from 3D Taylor-Green vortex simulations," University of Southampton, 2016. doi:10.5258/SOTON/401892.

[68] Jammy, S. P., Jacobs, C. T., and Sandham, N. D., "Performance evaluation of explicit finite difference algorithms with varying amounts of computational and memory intensity," *Journal of Computational Science*, 2016. doi:10.1016/j.jocs.2016.10.015.

[69] Sandberg, R. D., and Sandham, N. D., "Nonreflecting zonal characteristic boundary condition for direct numerical simulation of aerodynamic sound," *AIAA Journal*, Vol. 44, No. 2, 2006, pp. 402–405. doi:10.2514/1.19169.

[70] Chan, W. M., and Steger, J. L., "Enhancements of a three-dimensional hyperbolic grid generation scheme," *Applied Mathematics and Computation*, Vol. 51, No. 2-3, 1992, pp. 181–205. doi:10.1016/0096-3003(92)90073-a.

[71] Thompson, J. F., Soni, B. K., and Weatherill, N. P., *Handbook of grid generation*, CRC press, 1998.

[72] Jones, L. E., Sandberg, R. D., and Sandham, N. D., "Direct numerical simulations of forced and unforced separation bubbles on an airfoil at incidence," *Journal of Fluid Mechanics*, Vol. 602, 2008, pp. 175–207. doi:10.1017/S0022112008000864.

[73] Von Kármán, T., "Compressibility effects in aerodynamics," *Journal of the Aeronautical Sciences*, Vol. 8, No. 9, 1941, pp. 337–356. doi:10.2514/8.10737.

[74] Welch, P. D., "The use of fast Fourier transform for the estimation of power spectra: a method based on time averaging over short, modified periodograms," *IEEE Transactions on Audio and Electroacoustics*, Vol. 15, No. 2, 1967, pp. 70–73. doi:10.1109/TAU.1967.1161901.

[75] Moreau, S., Sanjosé, M., Lyu, B., and Ayton, L. J., "Analytical, numerical and experimental investigation of trailing-edge noise reduction on a Controlled Diffusion airfoil with serrations," *25th AIAA/CEAS Aeroacoustics Conference*, American Institute of Aeronautics and Astronautics, Delft, The Netherlands, 2019, p. 2450. doi:10.2514/6.2019-2450.

[76] Jones, L. E., Sandham, N. D., and Sandberg, R. D., "Acoustic source identification for transitional airfoil flows using cross correlations," *AIAA Journal*, Vol. 48, No. 10, 2010, pp. 2299–2312. doi:10.2514/1.J050345.

[77] Pierce, A. D., *Acoustics: An introduction to its physical principles and applications*, McGraw-Hill, 1981. doi:10.1007/978-3-030-11214-1.

[78] Sano, A., Abreu, L. I., Cavalieri, A. V. G., and Wolf, W. R., "Trailing-edge noise from the scattering of spanwise-coherent structures," *Physical Review Fluids*, Vol. 4, 2019, p. 094602. doi:10.1103/PhysRevFluids.4.094602.

[79] Amiet, R. K., "Noise due to turbulent flow past a trailing edge," *Journal of Sound and Vibration*, Vol. 47, No. 3, 1976, pp. 387–393. doi:10.1016/0022-460X(76)90948-2.

[80] Grasso, G., Roger, M., and Moreau, S., "Effect of sweep angle and of wall-pressure statistics on the free-field directivity of airfoil trailing-edge noise," *25th AIAA/CEAS Aeroacoustics Conference*, American Institute of Aeronautics and Astronautics, Delft, The Netherlands, 2019, p. 2612. doi:10.2514/6.2019-2612.